LIGHTWEIGHT DATASET PRUNING WITHOUT FULL TRAINING VIA EXAMPLE DIFFICULTY AND PREDICTION UNCERTAINTY

Yeseul Cho[*], **Baekrok Shin**[*], **Changmin Kang, Chulhee Yun**
Kim Jaechul Graduate School of AI, KAIST
{cyseul, br.shin, cmkang8128, chulhee.yun}@kaist.ac.kr

ABSTRACT

Recent advances in deep learning rely heavily on massive datasets, leading to substantial storage and training costs. Dataset pruning aims to alleviate this demand by discarding redundant examples. However, many existing methods require training a model with a full dataset over a large number of epochs before being able to prune the dataset, which ironically makes the pruning process more expensive than just training the model on the entire dataset. To overcome this limitation, we introduce a **Difficulty and Uncertainty-Aware Lightweight (DUAL)** score, which aims to identify important samples from the early training stage by considering both example difficulty and prediction uncertainty. To address a catastrophic accuracy drop at extreme pruning, we further propose a ratio-adaptive sampling using Beta distribution. Experiments on various datasets and learning scenarios such as image classification with label noise, image corruption, and model architecture generalization demonstrate the superiority of our method over previous state-of-the-art (SOTA) approaches. Specifically, on ImageNet-1k, our method reduces the time cost for pruning to 66% compared to previous methods while achieving a SOTA, specifically 60% test accuracy at a 90% pruning ratio. On CIFAR datasets, the time cost is reduced to just 15% while maintaining SOTA performance.

1 INTRODUCTION

Advancements in deep learning have been significantly driven by large-scale datasets. However, recent studies have revealed a power-law relationship between the generalization capacity of deep neural networks and the size of their training data (Hestness et al., 2017; Rosenfeld et al., 2019; Gordon et al., 2021), meaning that the improvement of model performance becomes increasingly cost-inefficient as we scale up the dataset size.

Fortunately, Sorscher et al. (2022) demonstrate that the power-law scaling of error can be reduced to exponential scaling with Pareto optimal data pruning. The main goal of dataset pruning is to identify and retain the most informative samples while discarding redundant data points for training neural networks. This approach can alleviate storage and computational costs as well as training efficiency.

However, many existing pruning methods require training a model with a full dataset over a number of epochs to measure the importance of each sample, which ironically makes the pruning process more expensive than just training the model once on the original large dataset. For instance, several score-based methods (Toneva et al., 2018; Pleiss et al., 2020; Paul et al., 2021; He et al., 2024; Zhang et al., 2024) require training as they utilize the dynamics from the whole training process. Some geometry-based methods, (Xia et al., 2022; Yang et al., 2024) leverage features from the penultimate layer of the trained model, therefore training a model is also required. Hybrid methods (Zheng et al., 2022; Maharana et al., 2023; Tan et al., 2025), which address the difficulty and diversity of samples simultaneously, still hold the same limitation as they use existing score metrics. Having to compute the dot product of learned features to get the neighborhood information makes them even more expensive to utilize.

[*] Authors contributed equally to this paper.

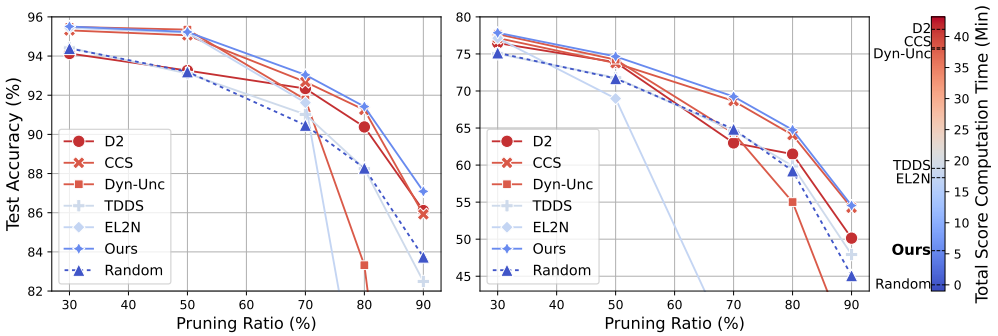

Figure 1: Test accuracy comparison on CIFAR datasets (**Left**: Results for CIFAR-10, **Right**: Results for CIFAR-100). The color represents the total computation time, including the time spent training the original dataset for score calculation, for each pruning method. Blue indicates lower computation time, while red indicates higher computation time. Our method demonstrates its ability to minimize computation time while maintaining SOTA performance.

To address this issue, we introduce **Difficulty and Uncertainty-Aware Lightweight** (**DUAL**) score, a metric that measures the importance of samples in the early stage of training by considering both prediction uncertainty and the example difficulty. Additionally, at the high pruning ratio—when the selected subset is scarce—we propose **pruning-ratio-adaptive Beta sampling**, which intentionally includes easier samples with lower scores to achieve a better representation of the data distribution (Sorscher et al., 2022; Zheng et al., 2022; Acharya et al., 2024).

Experiments conducted on CIFAR and ImageNet datasets under various learning scenarios verify the superiority of our method over previous SOTA methods. Specifically, on ImageNet-1k, our method reduces the time cost to 66% compared to previous methods while achieving a SOTA 60% test accuracy at the pruning ratio of 90%. On the CIFAR datasets, as illustrated in Figure 1, our method reduces the time cost to just 15% while maintaining SOTA performance. Especially, our method shows a notable performance when artificial noise is added.

2 Related Works

Data pruning aims to remove redundant examples, keeping the most informative subset of samples, namely the coreset. Research in this area can be broadly categorized into two groups: *score-based* and *geometry-based* methods. Score-based methods define metrics representing the difficulty or importance of data points to prioritize samples with high scores. Geometry-based methods, whereas, focus more on keeping a good representation of the true data distribution. Recent studies proposed *hybrid* methods that incorporate the example difficulty score with the diversity of coreset.

Score-based. EL2N (Paul et al., 2021) calculates $L2$ norms of the error vector as an approximation of the gradient norm. Entropy (Coleman et al., 2020) quantifies the information contained in the predicted probabilities at the end of training. However, the outcomes of such "snapshot" methods differ significantly from run to run, making it difficult to obtain a reliable score in a single run, as can be seen in Figure 7, Appendix B.

Methods using training dynamics offer more reliability as they incorporate information throughout an entire run of training. Forgetting (Toneva et al., 2018) score counts the number of forgetting events, a correct prediction on a data point is flipped to a wrong prediction during training. AUM (Pleiss et al., 2020) accumulates the gap between the target probability and the second-highest prediction probability. Dyn-Unc (He et al., 2024), which strongly inspired our approach, prioritizes the uncertain samples rather than typical easy samples or hard ones during model training. The prediction uncertainty is measured by the variation of predictions in a sliding window, and the score averages the variation throughout the whole training process. TDDS (Zhang et al., 2024) averages differences of Kullback-Leibler divergence loss of non-target probabilities for T training epochs, where T is highly dependent on the pruning ratio. Taking the training dynamics into account proves useful for pruning because it allows one to differentiate informative but hard samples from ones with

label noise (He et al., 2024). However, despite the stability and effectiveness of these methods, they fail to provide cost-effectiveness as it requires training the model on the entire dataset.

Geometry-based. Geometry-based methods focus on reducing redundancy among selected samples to provide better representation. SSP (Sorscher et al., 2022) selects the samples most distant from k-means cluster centers, while Moderate (Xia et al., 2022) focuses on samples with scores near the median. However, these methods often compromise generalization performance, as they underestimate the effectiveness of difficult examples.

Recently, hybrid approaches have emerged that harmonize both difficulty and diversity. CCS Zheng et al. (2022) partitions difficulty scores into bins and selects an equal number of samples from each bin to ensure a balanced representation. $\mathbb{D}^2$ Maharana et al. (2023) employs a message-passing mechanism with a graph structure where nodes represent difficulty scores and edges encode neighboring representations, facilitating effective sample selection. BOSS Acharya et al. (2024) introduces a Beta function for sampling based on difficulty scores, which resembles our pruning ratio-adaptive sampling; we discuss the key difference in Section 3.3. Our DUAL pruning is a score-based approach as it considers difficulty and uncertainty by the score metric. Additionally, diversity is introduced through our proposed Beta sampling, making it a hybrid approach.

3 Proposed Methods

3.1 Preliminaries

Let $\mathcal{D} \coloneqq \{(\boldsymbol{x}_1, y_1), \cdots, (\boldsymbol{x}_n, y_n)\}$ be a labeled dataset of n training samples, where $\boldsymbol{x} \in \mathcal{X} \subset \mathbb{R}^d$ and $y \in \mathcal{Y} \coloneqq \{1, \cdots, C\}$ are the data point and the label, respectively. C is a positive integer and indicates the number of classes. For each labeled data point $(\boldsymbol{x}, y) \in \mathcal{D}$, denote $\mathbb{P}_k(y \mid \boldsymbol{x})$ as the prediction probability of y given $\boldsymbol{x}$, for the model trained with k epochs. Let $\mathcal{S} \subset \mathcal{D}$ be the subset retained after pruning. Pruning ratio r is the ratio of the size of $\mathcal{D} \setminus \mathcal{S}$ to $\mathcal{D}$, or $r = 1 - \frac{|\mathcal{S}|}{|\mathcal{D}|}$.

The Dynamic Uncertainty (Dyn-Unc) score (He et al., 2024) prefers the most uncertain samples rather than easy-to-learn or hard-to-learn samples during model training. The uncertainty score is defined as the average of prediction variance throughout training. They first define the uncertainty in a sliding window of length J:

$$\mathrm{U}_k(\boldsymbol{x}, y) \coloneqq \sqrt{\frac{\sum_{j=0}^{J-1} \left[\mathbb{P}_{k+j}(y \mid \boldsymbol{x}) - \bar{\mathbb{P}}_k\right]^2}{J-1}} \tag{1}$$

where $\bar{\mathbb{P}}_k := \frac{\sum_{j=0}^{J-1} \mathbb{P}_{k+j}(y|\boldsymbol{x})}{J}$ is the average prediction of the model over the window $[k, k+J-1]$. Then taking the average of the uncertainty throughout the whole training process leads to the Dyn-Unc score:

$$\mathrm{U}(\boldsymbol{x}, y) = \frac{\sum_{k=1}^{T-J+1} \mathrm{U}_k(\boldsymbol{x}, y)}{T-J+1}. \tag{2}$$

3.2 Difficulty & Uncertainty-Aware Lightweight Score

Following the approach of Swayamdipta et al. (2020) and He et al. (2024), we analyze data points from ImageNet-1k based on the mean and standard deviation of predictions during training, as shown in Figure 2. We observe data points typically "flow" along the "moon" from bottom to top direction. Data points starting from the bottom-left region with a low prediction mean and low standard deviation move to the middle region with increased mean and standard deviation, and those starting in the middle region drift toward the upper-left region with a high prediction mean and smaller standard deviation. This phenomenon is closely aligned with existing observations that neural networks typically learn easy samples first, then treat harder samples later (Bengio et al., 2009; Arpit et al., 2017; Jiang et al., 2020; Shen et al., 2022). In other words, we see that the uncertainty of easy samples rises first, and then more difficult samples start to move and show an increased uncertainty score.

Figure 2 further gives a justification for this intuition. In Figure 2a, samples with the highest Dyn-Unc scores calculated at epoch 60 move upward by the end of training at epoch 90. It means that if

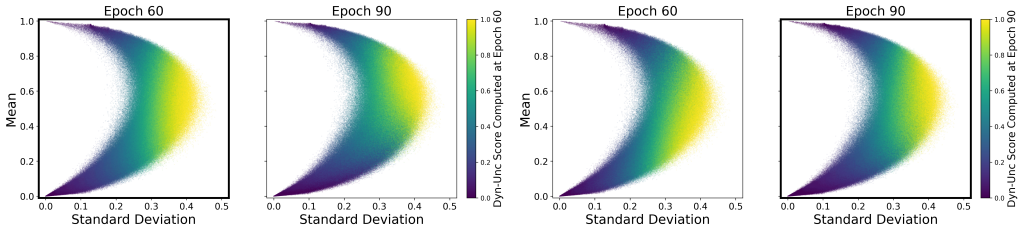

(a) Dyn-Unc score calculated at epoch $T = 60$. (b) Dyn-Unc score calculated at epoch $T = 90$.

Figure 2: The left column visualizes the prediction mean and standard deviation for each data point collected up to epoch 60, while the right column stands for epoch 90. Samples are colored by normalized Dyn-Unc score for each row. The expected cases of the original Dyn-Unc, where the score computation time step is the same as the final epoch of training, are marked with bold outlines.

we measure the Dyn-Unc score at the early stage of training, it gives the highest scores to relatively easy samples rather than the most informative samples. It seems undesirable that it results in poor test accuracy on its coreset as shown in Figure 8 of Appendix B.

To capture the most useful samples that are likely to contribute significantly to dynamic uncertainty during the whole training process (of 90 epochs) at the earlier training stage ($e.g.$ epoch of 60), we need to target the samples located near the bottom-right region of the moon-shaped distribution, as Figure 2b illustrates. Inspired by this observation, we propose a scoring metric that identifies such samples by taking the *uncertainty of the predictions* and the *prediction probability* into consideration.

Here, we propose the **Difficulty and Uncertainty-Aware Lightweight (DUAL) score**, a measure that unites example difficulty and prediction uncertainty. We define the DUAL score of a data point $(\boldsymbol{x}, y)$ at $k \in [T - J + 1]$ as

$$\mathrm{DUAL}_k(\boldsymbol{x}, y) \coloneqq \underbrace{\left(1 - \bar{\mathbb{P}}_k\right)}_{(a)} \underbrace{\sqrt{\frac{\sum_{j=0}^{J-1} \left[\mathbb{P}_{k+j}(y \mid \boldsymbol{x}) - \bar{\mathbb{P}}_k\right]^2}{J-1}}}_{(b)} \tag{3}$$

where $\bar{\mathbb{P}}_k := \frac{\sum_{j=0}^{J-1} \mathbb{P}_{k+j}(y|\boldsymbol{x})}{J}$ is the average prediction of the model over the window $[k, k + J - 1]$. Note that DUAL_k is the product of two terms: (a) $1 - \bar{\mathbb{P}}_k$ quantifies the example difficulty averaged over the window; (b) is the standard deviation of the prediction probability over the same window, estimating the prediction uncertainty.

Finally, the DUAL score of $(\boldsymbol{x}, y)$ is defined as the mean of DUAL_k scores over all windows:

$$\mathrm{DUAL}(\boldsymbol{x}, y) = \frac{\sum_{k=1}^{T-J+1} \mathrm{DUAL}_k(\boldsymbol{x}, y)}{T - J + 1}. \tag{4}$$

The DUAL score reflects training dynamics by leveraging prediction probability across several epochs It provides a reliable estimation to identify the most uncertain examples.

A theoretical analysis of a toy example further verifies the intuition above. Consider a linearly separable binary classification task $\{(\boldsymbol{x}_i \in \mathbb{R}^n, y_i \in \{\pm 1\})\}_{i=1}^N$, where $N = 2$ with $\|\boldsymbol{x}_1\| \ll \langle \boldsymbol{x}_1, \boldsymbol{x}_2 \rangle < \|\boldsymbol{x}_2\|$. Without loss of generality, we set $y_1 = y_2 = +1$. A linear classifier, $f(\boldsymbol{x}; \boldsymbol{w}) = \boldsymbol{w}^\top \boldsymbol{x}$, is employed as the model in our analysis. The parameter $\boldsymbol{w}$ is initialized at zero and updated by gradient descent. Soudry et al. (2018) prove that the parameter of linear classifiers diverges to infinity, but directionally converges to the L_2 maximum margin separator. This separator is determined by the support vectors closest to the decision boundary. If a valid pruning method encounters this task, then it should retain the point closer to the decision boundary, which is $\boldsymbol{x}_1$ in our case, and prune $\boldsymbol{x}_2$.

Due to its large norm, $\boldsymbol{x}_2$ exhibits higher score values in the early training stage for both uncertainty and DUAL scores. It takes some time for the model to predict $\boldsymbol{x}_1$ with high confidence, which increases its uncertainty level and prediction mean, as well as for scores of $\boldsymbol{x}_1$ to become larger than

$\boldsymbol{x}_2$ as training proceeds. In Theorem 3.1, we show through a rigorous analysis that the moment of such a flip in order happens strictly earlier for DUAL than dynamic uncertainty.

Theorem 3.1 (Informal)**.** *Define $\sigma(z) := (1+e^{-z})^{-1}$. Let $V_{t;J}^{(i)}$ be the variance and $\mu_{t;J}^{(i)}$ be the mean of $\sigma(f(\boldsymbol{x}_i;\boldsymbol{w}_t))$ within a window from time t to $t+J$. Denote T_v and T_{vm} as the first time step when $V_{t;J}^{(1)} > V_{t;J}^{(2)}$ and $V_{t;J}^{(1)}(1-\mu_{t;J}^{(i)}) > V_{t;J}^{(2)}(1-\mu_{t;J}^{(2)})$ occur, respectively. If the learning rate is small enough, then $T_{vm} < T_v$.*

Technical details about Theorem 3.1 are provided in Appendix D, together with an empirical verification of the time-efficiency of DUAL pruning over Dyn-Unc.

Empirically, as shown in Figure 3, the DUAL score targets data points in the bottom-right region during the early training phase, which eventually evolve to the middle-rightmost part by the end of training. This verifies that DUAL pruning identifies the most uncertain region faster than Dyn-Unc *both in theory and practice*. The distinction arises from the additional consideration of an example difficulty in our method. We believe that this adjustment leads to improved generalization performance compared to Dyn-Unc, as verified through various experiments in later sections.

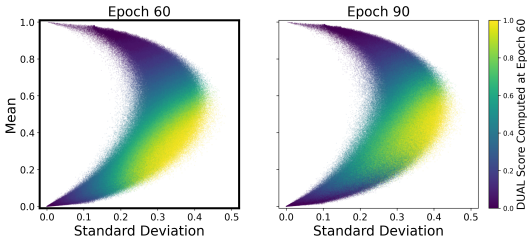

Figure 3: DUAL score also targets uncertain samples during the early epoch. In the end, selected samples are finally located in the most uncertain region.

However, score-based methods, including our method, suffer from limitations due to biased representations, leading to poor coreset test accuracy at high pruning ratios. To address this, we propose an additional strategy to adaptively select samples according to a ratio for pruning.

3.3 Pruning Ratio-Adaptive Sampling

Since the distribution of difficulty scores is dense in high-score samples, selecting only the highest-score samples may result in a biased model (Zhou et al., 2023; Maharana et al., 2023; Choi et al., 2024). To address this, we design a sampling method to determine the subset $\mathcal{S} \subset \mathcal{D}$, rather than simply pruning the samples with the lowest score. We introduce a Beta distribution that varies with the pruning ratio. The primary objective of this method is to ensure that the selected subsets gradually include more easy samples into the coreset as the pruning ratio increases.

However, the concepts of "easy" and "hard" cannot be distinguished solely based on uncertainty, or DUAL score. To address this, we use the *prediction mean* again for sampling. We utilize the Beta probability density function (PDF) to define the selection probability of each sample. First, we assign each data point a corresponding PDF value based on its prediction mean and weight this probability using the DUAL score. The weighted probability with the DUAL score is then normalized so that the sum equals 1, and then used as the sampling probability. To be clear, sampling probability is for selecting samples, *not for pruning*. Therefore, for each pruning ratio r, we randomly select $(1-r)\cdot n$ samples without replacement, where sampling probabilities are given according to the prediction mean and DUAL score as described. The detailed algorithm for our proposed pruning method with Beta sampling is provided in Algorithm 1, Appendix C.

We design the Beta PDF to assign a sampling probability concerning a prediction mean as follows:

$$\begin{aligned} \beta_r &= C \cdot (1-\mu_{\mathcal{D}})\,(1-r^{c_{\mathcal{D}}}) \\ \alpha_r &= C - \beta_r, \end{aligned} \tag{5}$$

where $C > 0$ is a fixed constant, and the μ_D stands for the prediction mean of the highest score sample. Recalling that the mean of Beta distribution is $\frac{\alpha_r}{\alpha_r+\beta_r}$, the above choice makes the mean of Beta distribution move progressively with r, starting from $\mu_{\mathcal{D}}$ ($r \simeq 0$, small pruning ratio) to one. In other words, with growing r, this Beta distribution becomes skewed towards the easier region ($r \to 1$, large pruning ratio), which in turn gives more weight to easy samples. The tendency of evolution should be different with datasets, thus a hyperparameter $c_{\mathcal{D}} \geq 1$ is used to control the rate

Table 1: Comparison of test accuracy between the DUAL score method and existing coreset selection techniques using ResNet-18 on CIFAR-10 and CIFAR-100 datasets. Training the model on the full dataset achieves an average test accuracy of 95.30% on CIFAR-10 and 78.91% on CIFAR-100. The best result in each pruning ratio is highlighted in bold.

Dataset (→)	**CIFAR-10**					**CIFAR-100**				
Pruning Rate (→)	**30%**	**50%**	**70%**	**80%**	**90%**	**30%**	**50%**	**70%**	**80%**	**90%**
Random	94.39±0.23	93.20±0.12	90.47±0.17	88.28±0.17	83.74±0.21	75.15±0.28	71.68±0.31	64.86±0.39	59.23±0.62	45.09±1.26
Entropy	93.48±0.06	92.47±0.17	89.54±0.18	88.53±0.19	82.57±0.36	75.20±0.25	70.90±0.35	61.70±0.47	56.24±0.51	42.25±0.39
Forgetting	95.48±0.14	94.94±0.21	89.55±0.65	75.47±1.27	46.64±1.90	77.52±0.26	70.93±0.37	49.66±0.20	39.09±0.41	26.87±0.73
EL2N	95.44±0.06	95.19±0.11	91.62±0.14	74.70±0.45	38.74±0.75	77.13±0.23	68.98±0.35	34.59±0.48	19.52±0.79	8.89 ±0.28
AUM	90.62±0.09	87.26±0.11	81.28±0.26	76.58±0.35	67.88±0.53	74.34±0.14	69.57±0.21	61.12±0.20	55.80±0.33	45.00±0.37
Moderate	94.26±0.09	92.79±0.09	90.45±0.21	88.90±0.17	85.52±0.29	75.20±0.25	70.90±0.35	61.70±0.47	56.24±0.51	42.25±0.39
Dyn-Unc	95.49±0.21	**95.35**±0.12	91.78±0.65	83.32±0.94	59.67±1.79	77.67±0.14	74.23±0.22	64.30±0.13	55.01±0.55	34.57±0.69
TDDS	94.42±0.13	93.11±0.14	91.02±0.19	88.25±0.24	82.49±0.28	75.02±0.37	71.80±0.33	64.61±0.24	59.88±0.21	47.93±0.21
CCS	95.31±0.22	95.06±0.15	92.68±0.17	91.25±0.21	85.92±0.39	77.15±0.28	73.83±0.21	68.65±0.31	64.06±0.21	54.23±0.48
D2	94.13±0.20	93.26±0.16	92.34±0.18	90.38±0.34	86.11±0.21	76.47±0.29	73.88±0.28	62.99±0.28	61.48±0.34	50.14±0.90
DUAL	95.25±0.17	94.95±0.22	91.75±0.98	82.02±1.85	54.95±0.42	77.43±0.18	74.62±0.47	66.41±0.52	56.57±0.57	34.38±1.39
DUAL+β sampling	**95.51**±0.06	95.23±0.08	**93.04**±0.43	**91.42**±0.35	**87.09**±0.36	**77.86**±0.12	**74.66**±0.12	**69.25**±0.22	**64.76**±0.23	**54.54**±0.09

of evolution of the Beta distribution. Specifically, the choice of $c_{\mathcal{D}}$ depends on the complexity of the initial dataset. For smaller and more complex datasets, setting $c_{\mathcal{D}}$ to a smaller value retains more easy samples. For larger and simpler datasets, setting $c_{\mathcal{D}}$ to a larger value allows more uncertain samples to be selected. (For your intuitive understanding, please refer to Figure 15 and Figure 16 in the Appendix C.) This is also aligned with the previous findings from Sorscher et al. (2022); if the initial dataset is small, the coreset is more effective when it contains easier samples, while for a relatively large initial dataset, including harder samples can improve generalization performance.

Remark. BOSS (Acharya et al., 2024) also uses the Beta distribution to sample easier data points during pruning, similar to our approach. However, a key distinction lies in how we define the Beta distribution's parameters, α_r and β_r. While BOSS adjusts these parameters to make the mode of the Beta distribution's PDF scale linearly with the pruning ratio r, we employ a non-linear combination. This non-linear approach has the crucial advantage of maintaining an almost stationary PDF at low pruning ratios. This stability is especially beneficial when the dataset becomes easier, where there is no need to focus on easy examples. Furthermore, unlike previous methods, we define PDF values based on the prediction mean, rather than any difficulty score, which is another significant difference.

4 Experiments

4.1 Experimental Settings

We assessed the performance of our proposed method in three key scenarios: image classification, image classification with noisy labels and corrupted images. In addition, we validate cross-architecture generalization on three-layer CNN, VGG-16 (Simonyan & Zisserman, 2015), ResNet-18 and ResNet-50 (He et al., 2015).

Hyperparameters. For training CIFAR-10 and CIFAR-100, we train ResNet-18 for 200 epochs with a batch size of 128. SGD optimizer with momentum of 0.9 and weight decay of 0.0005 is used. The learning rate is initialized as 0.1 and decays with the cosine annealing scheduler. As Zhang et al. (2024) show that smaller batch size boosts performance at high pruning rates, we also halved the batch size for 80% pruning, and for 90% we reduced it to one-fourth. For ImageNet-1k, ResNet-34 is trained for 90 epochs with a batch size of 256 across all pruning ratios. An SGD optimizer with a momentum of 0.9, a weight decay of 0.0001, and an initial learning rate of 0.1 is used, combined with a cosine annealing scheduler.

Baselines. The baselines considered in this study are listed as follows[1]: (1) Random; (2) Entropy (Coleman et al., 2020); (3) Forgetting (Toneva et al., 2018); (4) EL2N (Paul et al., 2021); (5) AUM (Pleiss et al., 2020); (6) Moderate (Xia et al., 2022); (7) Dyn-Unc (He et al., 2024); (8) TDDS (Zhang et al., 2024); (9) CCS (Zheng et al., 2022); and (10) $\mathbb{D}^2$ (Maharana et al., 2023). To

[1]Infomax (Tan et al., 2025) was excluded as it employs different base hyperparameters in the original paper compared to other baselines and does not provide publicly available code. See Appendix A.1 for more discussion.

ensure a fair comparison, all methods were trained with the same base hyperparameters for training, and the best hyperparameters reported in their respective original works for scoring. Technical details are provided in the Appendix A.1.

4.2 Image Classification Benchmarks

Table 1 presents the test accuracy for image classification results on CIFAR-10 and CIFAR-100. Our pruning method consistently outperforms other baselines, particularly when combined with Beta sampling. While the DUAL score exhibits competitive performance in lower pruning ratios, its accuracy degrades with more aggressive pruning. Our Beta sampling effectively mitigates this performance drop.

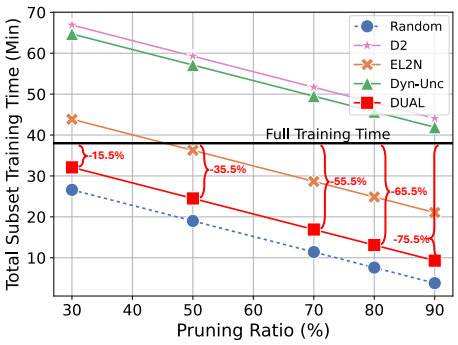

Figure 4: Comparison in total time spent on CIFAR datasets.

Notably, the DUAL score only requires training a single model for *only 30 epochs*, significantly reducing the computational cost. In contrast, the second-best methods, Dyn-Unc and CCS, rely on scores computed over a full 200-epoch training cycle, making them considerably less efficient. Even considering subset selection, score computation, and subset training, the total time remains less than a single full training run, as shown in Figure 4. Specifically, on CIFAR-10, our method achieves lossless pruning up to a 50% pruning ratio while saving 35.5% of total training time.

Table 2: Comparison of test accuracy of DUAL score with existing coreset selection methods using ResNet34 for ImageNet-1k. The model trained with the full dataset achieves 73.1% test accuracy. The best result in each pruning ratio is highlighted in bold.

Pruning Rate	**30%**	**50%**	**70%**	**80%**	**90%**
Random	72.2	70.3	66.7	62.5	52.3
Entropy	72.3	70.8	64.0	55.8	39.0
Forgetting	72.6	70.9	66.5	62.9	52.3
EL2N	72.2	67.2	48.8	31.2	12.9
AUM	72.5	66.6	40.4	21.1	9.9
Moderate	72.0	70.3	65.9	61.3	52.1
Dyn-Unc	70.9	68.3	63.5	59.1	49.0
TDDS	70.5	66.8	59.4	54.4	46.0
CCS	72.3	70.5	67.8	64.5	57.3
D2	72.9	71.8	68.1	65.9	55.6
DUAL	72.8	71.5	68.6	64.7	53.1
DUAL+β sampling	**73.3**	**72.3**	**69.4**	**66.5**	**60.0**

We also evaluate our pruning method on the large-scale dataset, ImageNet-1k. The DUAL score is computed during training, specifically at epoch 60, which is 33% earlier than the original train epoch used to compute scores for other baseline methods. As shown in Table 2, Dyn-Unc performs worse than random pruning across all pruning ratios, and we attribute this undesirable performance to its limited total training epochs (only 90), which is insufficient for Dyn-Unc to fully capture the training dynamics of each sample. In contrast, our DUAL score, combined with Beta sampling, outperforms all competitors while requiring the least computational cost. The DUAL score's ability to consider both training dynamics and the difficulty of examples enables it to effectively identify uncertain samples early in the training process, even when training dynamics are limited. Remarkably, for 90% pruned Imagenet-1K, it maintains a test accuracy of 60.0%, surpassing the previous state-of-the-art (SOTA) by a large margin.

4.3 Experiments under More Realistic Scenarios

4.3.1 Label Noise and Image Corruption

Data affected by label noise or image corruption are difficult and unnecessary samples that hinder model learning and degrade generalization performance. Therefore, filtering out these samples

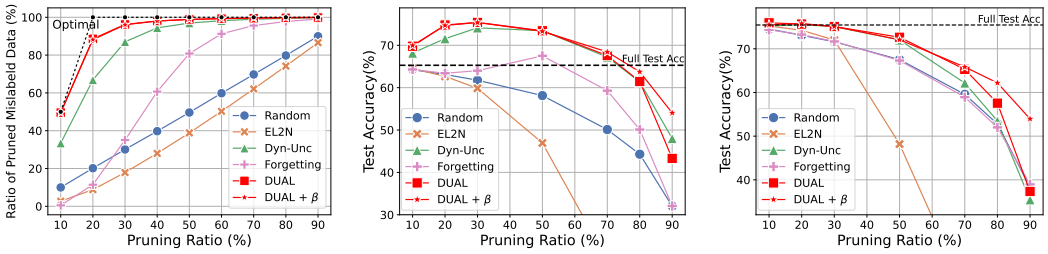

(a) Pruned mislabeled data ratio (b) Test accuracy under label noise (c) Test accuracy under image noise

Figure 5: The left figure shows the ratio of pruned mislabeled data under 20% label noise on CIFAR-100 trained with ResNet-18. When label noise is 20%, the optimal value (black dashed line) corresponds to pruning 100% of mislabeled data at a 20% pruning ratio. The middle and right figures depict test accuracy under 20% label noise and 20% image corruption, respectively. Our method effectively prunes mislabeled data near the optimal value while maintaining strong generalization performance. Results are averaged over five random seeds.

through data pruning is crucial. Most data pruning methods, however, either focus solely on selecting difficult samples based on example difficulty (Paul et al., 2021; Pleiss et al., 2020; Coleman et al., 2020) or prioritize dataset diversity (Zheng et al., 2022; Xia et al., 2022), making them unsuitable for effectively pruning such noisy and corrupted samples.

In contrast, methods that select uncertain samples while considering training dynamics, such as Forgetting (Toneva et al., 2018) and Dyn-Unc (He et al., 2024), demonstrate robustness by pruning both the hardest and easiest samples, ultimately improving generalization performance, as illustrated in Figure 5a. However, since noisy samples tend to be memorized after useful samples are learned (Arpit et al., 2017; Jiang et al., 2020), there is a possibility that those noisy samples may still be treated as uncertain in the later stages of training and thus be included in the selected subset.

The DUAL score aims to identify high-uncertainty samples early in training by considering both training dynamics and example difficulty. Noisy data, typically under-learned compared to other challenging samples during this phase, exhibit lower uncertainty (Figure 11, Appendix B.1). Consequently, our method effectively prunes these noisy samples.

To verify this, we evaluate our method by introducing a specific proportion of symmetric label noise (Patrini et al., 2017; Xia et al., 2020; Li et al., 2022) and applying five different types of image corruptions (Wang et al., 2018; Hendrycks & Dietterich, 2019; Xia et al., 2021). We use CIFAR-100 with ResNet-18 and Tiny-ImageNet with ResNet-34 for these experiments. On CIFAR-100, we test label noise and image corruption ratios of 20%, 30%, and 40%. For Tiny-ImageNet, we use a 20% ratio of label noise and image corruption. We prune the label noise-added dataset using a model trained for 50 epochs and the image-corrupted dataset with a model trained for 30 epochs using DUAL pruning—both significantly lower than the 200 epochs used by other methods. For detailed experimental settings, please refer to Appendix A.2. As shown in Figure 5, the left plot demonstrates that DUAL pruning effectively removes mislabeled data at a ratio close to the optimal. Notably, when the pruning ratio is 10%, nearly *all pruned samples are mislabeled data*. Consequently, as observed in Figure 5b, DUAL pruning leads to improved test accuracy compared to training on the full dataset, even up to a pruning ratio of 70%. At lower pruning ratios, performance improves as mislabeled data are effectively removed, highlighting the advantage of our approach in handling label noise. Similarly, for image corruption, our method prunes more corrupted data across all corruption rates compared to other methods, as shown in Figure 13, 14 in Appendix B.2. As a result, this leads to higher test accuracy, as demonstrated in Figure 5c.

Detailed results, including exact numerical values for different corruption rates and Tiny-ImageNet experiments, can be found in Appendix B.1 and B.2. Across all experiments, DUAL pruning consistently shows *strong noise robustness* and outperforms other methods by a substantial margin.

4.3.2 Cross-Architecture Generalization

We also evaluate the ability to transfer scores across various model architectures. To be specific, if we can get high-quality example scores for pruning by using a simpler architecture than one

Table 3: Cross-architecture generalization performance on CIFAR-100 from ResNet-18 to ResNet-50. We report an average of five runs. 'R50 → R50' stands for score computation on ResNet-50, as a baseline.

	ResNet-18 → ResNet-50			
Pruning Rate (→)	30%	50%	70%	90%
Random	74.47 ±0.67	70.09 ±0.42	60.06 ±0.99	41.91 ±4.32
EL2N	76.42 ±1.00	69.14 ±1.00	45.16 ±3.21	19.63 ±1.15
Dyn-Unc	77.31 ±0.34	72.12 ±0.68	59.38 ±2.35	31.74 ±2.31
CCS	74.78 ±0.66	69.98 ±1.18	59.75 ±1.41	41.54 ±3.94
DUAL	**78.03** ±0.83	72.82 ±1.46	63.08 ±2.45	33.65 ±2.92
DUAL +β	77.82 ±0.65	**73.98** ±0.62	**66.36** ±1.66	**49.90** ±2.56
DUAL (R50→R50)	77.82 ±0.64	73.66 ±0.85	52.12 ±2.73	26.13 ±1.96
DUAL (R50→R50)+β	77.57 ±0.23	73.44 ±0.87	65.17 ±0.96	47.63 ±2.47

for the training, our DUAL pruning would become even more efficient in time and computational cost. Therefore, we focus on the cross-architecture generalization from relatively small networks to larger ones with three-layer CNN, VGG-16, ResNet-18, and ResNet-50. Competitors are selected from each categorized group of the pruning approach: EL2N from difficulty-based, Dyn-Unc from uncertainty-based, and CCS from the geometry-based group.

For instance, we get training dynamics from the ResNet-18 and then calculate the example scores. Then, we prune samples using scores calculated from ResNet-18, and train selected subsets on ResNet-50. The result with ResNet-18 and ResNet-50 is described in Table 3. Surprisingly, the coreset shows competitive performance to the baseline, where the baseline refers to the test accuracy after training a coreset constructed based on the score calculated from ResNet-50. For all pruning cases, we observe that our methods reveal the highest performances. Specifically, when we prune 70% and 90% of the original dataset, we find that all other methods fail, showing worse test accuracies than random pruning.

We also test the cross-architecture generalization performance with three-layer CNN, VGG-16, and ResNet-18 in Appendix B.3. Even for a simple model like three-layer CNN, we see our methods show consistent performance, as can be seen in Table 13 in Appendix B.3. This observation gives rise to an opportunity to develop some small proxy networks to get example difficulty with less computational cost. Transfer across models with similar capacities, $e.g.$ from VGG-16 to ResNet-18 and vice versa, also supports the verification of cross-architecture compatibility.

4.4 Ablation Studies

Hyperparameter Analysis. Here, we investigate the robustness of our hyperparameters, T, J, and $c_{\mathcal{D}}$. We fix J across all experiments, as it has minimal impact on selection, indicating its robustness (Fig 9, Appendix B). In Figure 6, we assess the robustness of T by varying it from 20 to 200 on CIFAR-100. We find that while T remains highly robust in earlier epochs, increasing T degrades generalization performance. This is expected, as larger T overemphasizes difficult samples due to our difficulty-aware selection. Thus, pruning in earlier epochs (from 30 to 50) proves to be more effective and robust. For the $c_{\mathcal{D}}$, we vary it from 3 to 7 and find robustness, especially in the aggressive pruning regime. All results are averaged across three runs.

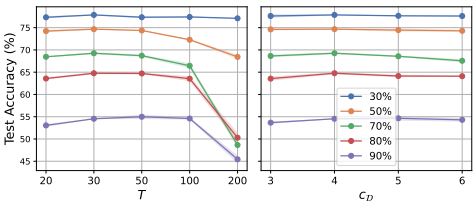

Figure 6: **Left**: Varying T with $J = 10$ and $c_{\mathcal{D}} = 4$. **Right**: Varying $c_{\mathcal{D}}$ with $T = 30$ and $J = 10$.

Beta Sampling Analysis. Next, we study the impact of our proposed pruning-ratio-adaptive Beta sampling on existing score metrics. We apply our Beta sampling strategy to prior score-based meth-

Table 4: Comparison on CIFAR-10 and CIFAR-100 for 90% pruning rate. We report average accuracy with five runs. The best performance is in bold in each column.

	CIFAR-10		CIFAR-100	
Method	Thresholding	β-Sampling	Thresholding	β-Sampling
Random	**83.74** ±0.21	83.31 (-0.43) ±0.14	**45.09** ±1.26	51.76 (+6.67) ±0.25
EL2N	38.74 ±0.75	87.00 (+48.26) ±0.45	8.89 ±0.28	53.97 (+45.08) ±0.63
Forgetting	46.64 ±1.90	85.67 (+39.03) ±0.13	26.87 ±0.73	52.40 (+25.53) ±0.43
Dyn-Unc	59.67 ±1.79	85.33 (+25.66) ±0.20	34.57 ±0.69	51.85 (+17.28) ±0.35
Ours	54.95 ±0.42	**87.09** (+32.14) ±0.36	34.28 ±1.39	**54.54** (+20.26) ±0.09

ods, including Forgetting, EL2N, and Dyn-Unc, using the CIFAR10 and CIFAR100 datasets. By comparing our sampling approach with vanilla threshold pruning, which selects only the highest-scoring samples, we observe that prior score-based methods become remarkably comparable to random pruning after Beta sampling is adjusted (see Table 4).

Even adapted for random pruning, our Beta sampling proves to perform well. Notably, EL2N, which performs poorly on its own, becomes significantly more effective when combined with our sampling method. Similar improvements are also seen with Forgetting and Dyn-Unc scores. This is because our proposed Beta sampling enhances the diversity of selected samples in turn, especially when used with example difficulty-based methods. More results conducted for 80% pruning cases are included in the Appendix B.4.

Additional Analysis. In addition to the main results presented in this paper, we also conducted various experiments to further explore the effectiveness of our method. These additional results include an analysis of coreset performance under a time budget ($e.g.$ other score metrics are also computed by using training dynamics up to epoch 30) and Spearman rank correlation was calculated between individual scores and the averaged score across five runs to assess the consistency of scores for each sample. Furthermore, additional results in extreme cases, 30% and 40% of label noise and image corruption can be found in Appendix B.

5 Conclusion

We introduce the Difficulty and Uncertainty-Aware Lightweight (DUAL) score, a novel scoring metric designed for cost-effective pruning. The DUAL score is the first metric to integrate both difficulty and uncertainty into a single measure, and its effectiveness in identifying the most informative samples early in training is further supported by theoretical analysis. Additionally, we propose pruning-ratio-adaptive sampling to account for sample diversity, particularly when the pruning ratio is extremely high. Our proposed pruning methods, DUAL score and DUAL score combined with Beta sampling demonstrate remarkable performance, particularly in realistic scenarios involving label noise and image corruption, by effectively distinguishing noisy samples.

Data pruning research has been evolving in a direction that contradicts its primary objective of reducing computational and storage costs while improving training efficiency. This is mainly because the computational cost of pruning often exceeds that of full training. By introducing our DUAL method, we take a crucial step toward overcoming this challenge by significantly reducing the computation cost associated with data pruning, making it feasible for practical scenarios. Ultimately, we believe this will help minimize resource waste and enhance training efficiency.

Acknowledgement

This work was supported by two Institute of Information & communications Technology Planning & Evaluation (IITP) grants (No. RS-2019-II190075, Artificial Intelligence Graduate School Program (KAIST); No. RS-2024-00457882, National AI Research Lab Project) funded by the Korean government (MSIT), and a National Research Foundation of Korea (NRF) grant (No. NRF-2019R1A5A1028324) funded by the Korean government (MSIT).

REFERENCES

Abhinab Acharya, Dayou Yu, Qi Yu, and Xumin Liu. Balancing feature similarity and label variability for optimal size-aware one-shot subset selection. In *Forty-first International Conference on Machine Learning*, 2024.

Devansh Arpit, Stanisław Jastrzębski, Nicolas Ballas, David Krueger, Emmanuel Bengio, Maxinder S Kanwal, Tegan Maharaj, Asja Fischer, Aaron Courville, Yoshua Bengio, et al. A closer look at memorization in deep networks. In *International conference on machine learning*, pp. 233–242. PMLR, 2017.

Yoshua Bengio, Jérôme Louradour, Ronan Collobert, and Jason Weston. Curriculum learning. In *Proceedings of the 26th annual international conference on machine learning*, pp. 41–48, 2009.

Hoyong Choi, Nohyun Ki, and Hye Won Chung. Bws: Best window selection based on sample scores for data pruning across broad ranges. *arXiv preprint arXiv:2406.03057*, 2024.

Cody Coleman, Christopher Yeh, Stephen Mussmann, Baharan Mirzasoleiman, Peter Bailis, Percy Liang, Jure Leskovec, and Matei Zaharia. Selection via proxy: Efficient data selection for deep learning, 2020. URL `https://arxiv.org/abs/1906.11829`.

Mitchell A Gordon, Kevin Duh, and Jared Kaplan. Data and parameter scaling laws for neural machine translation. In *ACL Rolling Review - May 2021*, 2021. URL `https://openreview.net/forum?id=IKA7MLxsLSu`.

Suriya Gunasekar, Jason D Lee, Daniel Soudry, and Nati Srebro. Implicit bias of gradient descent on linear convolutional networks. *Advances in neural information processing systems*, 31, 2018.

Kaiming He, Xiangyu Zhang, Shaoqing Ren, and Jian Sun. Deep residual learning for image recognition, 2015. URL `https://arxiv.org/abs/1512.03385`.

Muyang He, Shuo Yang, Tiejun Huang, and Bo Zhao. Large-scale dataset pruning with dynamic uncertainty. In *Proceedings of the IEEE/CVF Conference on Computer Vision and Pattern Recognition*, pp. 7713–7722, 2024.

Dan Hendrycks and Thomas Dietterich. Benchmarking neural network robustness to common corruptions and perturbations. *arXiv preprint arXiv:1903.12261*, 2019.

Joel Hestness, Sharan Narang, Newsha Ardalani, Gregory Diamos, Heewoo Jun, Hassan Kianinejad, Md Mostofa Ali Patwary, Yang Yang, and Yanqi Zhou. Deep learning scaling is predictable, empirically. *arXiv preprint arXiv:1712.00409*, 2017.

Ziheng Jiang, Chiyuan Zhang, Kunal Talwar, and Michael C Mozer. Characterizing structural regularities of labeled data in overparameterized models. *arXiv preprint arXiv:2002.03206*, 2020.

Shikun Li, Xiaobo Xia, Shiming Ge, and Tongliang Liu. Selective-supervised contrastive learning with noisy labels. In *Proceedings of the IEEE/CVF conference on computer vision and pattern recognition*, pp. 316–325, 2022.

Adyasha Maharana, Prateek Yadav, and Mohit Bansal. D2 pruning: Message passing for balancing diversity and difficulty in data pruning. *arXiv preprint arXiv:2310.07931*, 2023.

Giorgio Patrini, Alessandro Rozza, Aditya Krishna Menon, Richard Nock, and Lizhen Qu. Making deep neural networks robust to label noise: A loss correction approach. In *Proceedings of the IEEE conference on computer vision and pattern recognition*, pp. 1944–1952, 2017.

Mansheej Paul, Surya Ganguli, and Gintare Karolina Dziugaite. Deep learning on a data diet: Finding important examples early in training. *Advances in neural information processing systems*, 34:20596–20607, 2021.

Geoff Pleiss, Tianyi Zhang, Ethan R. Elenberg, and Kilian Q. Weinberger. Identifying mislabeled data using the area under the margin ranking, 2020. URL `https://arxiv.org/abs/2001.10528`.

Jonathan S Rosenfeld, Amir Rosenfeld, Yonatan Belinkov, and Nir Shavit. A constructive prediction of the generalization error across scales. *arXiv preprint arXiv:1909.12673*, 2019.

Ruoqi Shen, Sébastien Bubeck, and Suriya Gunasekar. Data augmentation as feature manipulation. In *International conference on machine learning*, pp. 19773–19808. PMLR, 2022.

Karen Simonyan and Andrew Zisserman. Very deep convolutional networks for large-scale image recognition, 2015. URL `https://arxiv.org/abs/1409.1556`.

Ben Sorscher, Robert Geirhos, Shashank Shekhar, Surya Ganguli, and Ari S. Morcos. Beyond neural scaling laws: beating power law scaling via data pruning. In Alice H. Oh, Alekh Agarwal, Danielle Belgrave, and Kyunghyun Cho (eds.), *Advances in Neural Information Processing Systems*, 2022. URL `https://openreview.net/forum?id=UmvSlP-PyV`.

Daniel Soudry, Elad Hoffer, Mor Shpigel Nacson, Suriya Gunasekar, and Nathan Srebro. The implicit bias of gradient descent on separable data. *Journal of Machine Learning Research*, 19(70): 1–57, 2018.

Swabha Swayamdipta, Roy Schwartz, Nicholas Lourie, Yizhong Wang, Hannaneh Hajishirzi, Noah A Smith, and Yejin Choi. Dataset cartography: Mapping and diagnosing datasets with training dynamics. In *Proceedings of the 2020 Conference on Empirical Methods in Natural Language Processing (EMNLP)*, pp. 9275–9293, 2020.

Haoru Tan, Sitong Wu, Wei Huang, Shizhen Zhao, and XIAOJUAN QI. Data pruning by information maximization. In *The Thirteenth International Conference on Learning Representations*, 2025. URL `https://openreview.net/forum?id=93XT0lKOct`.

Mariya Toneva, Alessandro Sordoni, Remi Tachet des Combes, Adam Trischler, Yoshua Bengio, and Geoffrey J Gordon. An empirical study of example forgetting during deep neural network learning. *arXiv preprint arXiv:1812.05159*, 2018.

Yisen Wang, Weiyang Liu, Xingjun Ma, James Bailey, Hongyuan Zha, Le Song, and Shu-Tao Xia. Iterative learning with open-set noisy labels. In *Proceedings of the IEEE conference on computer vision and pattern recognition*, pp. 8688–8696, 2018.

Xiaobo Xia, Tongliang Liu, Bo Han, Chen Gong, Nannan Wang, Zongyuan Ge, and Yi Chang. Robust early-learning: Hindering the memorization of noisy labels. In *International conference on learning representations*, 2020.

Xiaobo Xia, Tongliang Liu, Bo Han, Mingming Gong, Jun Yu, Gang Niu, and Masashi Sugiyama. Instance correction for learning with open-set noisy labels. *arXiv preprint arXiv:2106.00455*, 2021.

Xiaobo Xia, Jiale Liu, Jun Yu, Xu Shen, Bo Han, and Tongliang Liu. Moderate coreset: A universal method of data selection for real-world data-efficient deep learning. In *The Eleventh International Conference on Learning Representations*, 2022.

Shuo Yang, Zhe Cao, Sheng Guo, Ruiheng Zhang, Ping Luo, Shengping Zhang, and Liqiang Nie. Mind the boundary: Coreset selection via reconstructing the decision boundary. In *Forty-first International Conference on Machine Learning*, 2024.

Xin Zhang, Jiawei Du, Yunsong Li, Weiying Xie, and Joey Tianyi Zhou. Spanning training progress: Temporal dual-depth scoring (tdds) for enhanced dataset pruning. In *Proceedings of the IEEE/CVF Conference on Computer Vision and Pattern Recognition*, pp. 26223–26232, 2024.

Haizhong Zheng, Rui Liu, Fan Lai, and Atul Prakash. Coverage-centric coreset selection for high pruning rates. *arXiv preprint arXiv:2210.15809*, 2022.

Xiao Zhou, Renjie Pi, Weizhong Zhang, Yong Lin, and Tong Zhang. Probabilistic bilevel coreset selection, 2023. URL `https://arxiv.org/abs/2301.09880`.

A TECHNICAL DETAILS

A.1 DETAILS ON BASELINE IMPLEMENTATION

EL2N Paul et al. (2021) is defined as the error $L2$ norm between the true labels and predictions of the model. The examples with low scores are pruned out. We calculated error norms at epoch 20 from five independent runs, then the average was used for Ethe L2N score.

Forgetting Toneva et al. (2018) is defined as the number of forgetting events, where the model prediction goes wrong after the correct prediction, up until the end of training. Rarely unforgotten samples are pruned out.

AUM Pleiss et al. (2020) accumulates the margin, which means the gap between the target probabilities and the second largest prediction of a model. They calculate the margin at every epoch and then transform it into an AUM score at the end of the training. Here samples with small margins are considered as mislabeled samples, thus data points with small AUM scores are eliminated.

Entropy Coleman et al. (2020) is calculated as the entropy of prediction probabilities at the end of training, and then the samples that have high entropy are selected into coreset.

Dyn-Unc He et al. (2024) is also calculated at the end of training, with the window length J set as 10. Samples with high uncertainties are selected into the subset after pruning.

TDDS Zhang et al. (2024) adapts different hyperparameter for each pruning ratio. As they do not provide full information for implementation, we have no choice but to set parameters for the rest cases arbitrarily. The provided setting for (pruning ratio, computation epoch T, the length of sliding window K) is (0.3, 70, 10), (0.5, 90, 10), (0.7, 80, 10), (0.8, 30, 10), and (0.9, 10, 5) for CIFAR-100, and for ImageNet-(0.3, 20, 10), (0.5, 20, 10), (0.7, 30, 20). Therefore, we set the parameter for CIFAR-10 as the same as CIFAR-100, and for 80%, 90% pruning on ImageNet-1k, we set them as (30, 20), following the choice for 70% pruning.

CCS Zheng et al. (2022) for the stratified sampling method, we adapt the AUM score as the original CCS paper does. They assign different hard cutoff rates for each pruning ratio. For CIFAR-10, the cutoff rates are (30%, 0), (50%, 0), (70%, 10%), (80%, 10%), (90%, 30%). For CIFAR-100 and ImageNet-1k, we set them as the same as in the original paper.

D2 Maharana et al. (2023) for $\mathbb{D}^2$ pruning, we set the initial node using forgetting scores for CIFAR-10 and CIFAR-100, we set the number of neighbors k, and message passing weight γ the same as in the original paper.

Note that, Infomax (Tan et al., 2025) was excluded as it employs different base hyperparameters in the original paper compared to other baselines and does not provide publicly available code. Additionally, implementation details, such as the base score metric used to implement Infomax, are not provided. As we intend to compare other baseline methods with the same training hyperparameters, we do not include the accuracies of Infomax in our tables. To see if we can match the performance of Infomax, we tested our method with different training details. For example, if we train the subset using the same number of iterations (not epoch) as the full dataset and use a different learning rate tuned for our method, then an improved accuracy of 59% is achievable for 90% pruning on CIFAR-100, which surpasses the reported performance of Infomax. For the ImageNet-1k dataset, our method outperforms Infomax without any base hyperparameter tuning, while also being cost-effective.

A.2 DETAILED EXPERIMENTAL SETTINGS

Here we clarify the technical details of our work. For training the model on the full dataset and the selected subset, all parameters are used identically except for batch sizes. For CIFAR-10/100, we train ResNet-18 for 200 epochs with a batch size of 128, for each pruning ratio {30%, 50%, 70%, 80%, 90%} we use different batch sizes with {128, 128, 128, 64, 32}. We set the initial learning rate as 0.1, the optimizer as SGD with momentum 0.9, and the scheduler as cosine annealing scheduler with weight decay 0.0005. For training ImageNet, we use ResNet-34 as the network architecture. For all coresets with different pruning rates, we train models for 300,000 iterations with a 256 batch size. We use the SGD optimizer with 0.9 momentum and 0.0001 weight decay, using a 0.1

initial learning rate. The cosine annealing learning rate scheduler was used for training. For a fair comparison, we used the same parameters across all pruning methods, including ours. All experiments were conducted using an NVIDIA A6000 GPU.

For calculating the DUAL score, we need three parameters T, J, and $c_{\mathcal{D}}$, each means score computation epoch, the length of the sliding window, and hyperparameter regarding the training dataset. We fix J as 10 for all experiments. We use (T, J, $c_{\mathcal{D}}$) for each dataset as follows. For CIFAR-10, we use (30, 10, 5.5), for CIFAR-100, (30, 10, 4), and for ImageNet-1k, (60, 10, 11). We first roughly assign the term $c_{\mathcal{D}}$ based on the size of the initial dataset and by considering the relative difficulty of each, we set $c_{\mathcal{D}}$ for CIFAR-100 smaller than that of CIFAR-10. For the ImageNet-1k dataset, which contains 1,281,167 images, the size of the initial dataset is large enough that we do not need to set $c_{\mathcal{D}}$ to a small value to intentionally sample easier samples. Also, note that we fix the value of C of Beta distribution at 15 across all experiments. A more detailed distribution, along with visualization, can be found in Appendix C.

Experiments with label noise and image corruption on CIFAR-100 are conducted under the same settings as described above, except for the hyperparameters for DUAL pruning. For label noise experiments, we set T to 50 and J to 10 across all label noise ratios. For $c_{\mathcal{D}}$, we set it to 6 for 20% and 30% noise, 8 for 40% noise. For image corruption experiments, we set T to 30, J to 10, and $c_{\mathcal{D}}$ to 6 across all image corruption ratios.

For the Tiny-ImageNet case, we train ResNet-34 for 90 epochs with a batch size of 256 across all pruning ratios, using a weight decay of 0.0001. The initial learning rate is set to 0.1 with the SGD optimizer, where the momentum is set to 0.9, combined with a cosine annealing learning rate scheduler. For the hyperparameters used in DUAL pruning, we set T to 60, J to 10, and $c_{\mathcal{D}}$ to 6 for the label noise experiments. For the image corruption experiments, we set T to 60, J to 10, and $c_{\mathcal{D}}$ to 2. We follow the ImageNet-1k hyperparameters to implement the baselines.

B More Results on Experiments

We evaluate our proposed DUAL score through a wide range of analyses in this section. In Appendix B.1 and B.2, we demonstrate the robustness of the DUAL score across a variety of experiments. In Appendix B.3, we investigate the cross-architecture performance of DUAL pruning. In Appendix B.4, we show that beta sampling performs well even when combined with other score metrics, such as EL2N and Dyn-Unc, and also shows strong performance when compared to other sampling methods, especially CCS.

We first investigate the stability of our DUAL score compared to other baselines. We calculate the Spearman rank correlation of each score and the average score across five runs, following Paul et al. (2021). As shown in Figure 7, snapshot-based methods such as EL2N and Entropy exhibit relatively low correlation compared to methods that consider training dynamics. In particular, the DUAL score shows minimal score variation across runs, resulting in a high Spearman rank correlation, indicating strong stability across random seeds. Notably, even when the scores are calculated at the 30th epoch, the Spearman correlation between the individual scores and the overall average score remains approximately 0.95.

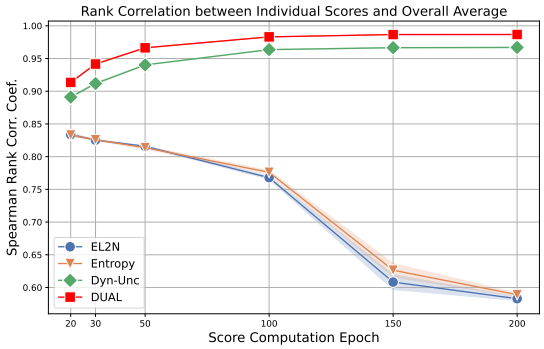

Figure 7: Average of Spearman rank correlation among independent runs and an overall average of five runs.

Next, we compute the Dyn-Unc, TDDS, and AUM scores at the 30th epoch, as we do for our method, and then compare the test accuracy on the coreset. Our pruning method, using the DUAL score and ratio-adaptive beta sampling, outperforms the others by a significant margin, as illustrated in Figure 8. We see using epoch 30 results in insufficient training dynamics for the others, thus it negatively impacts their performance.

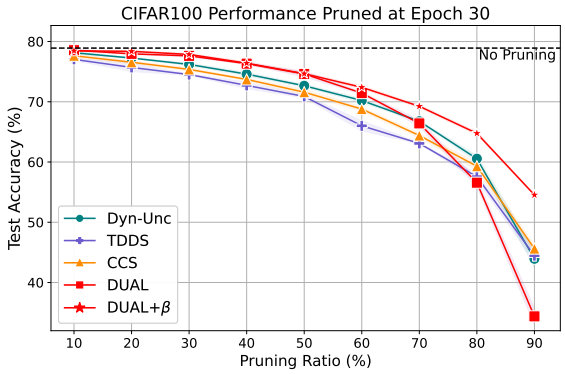

Figure 8: Test accuracy comparison under limited computation budget (epoch 30)

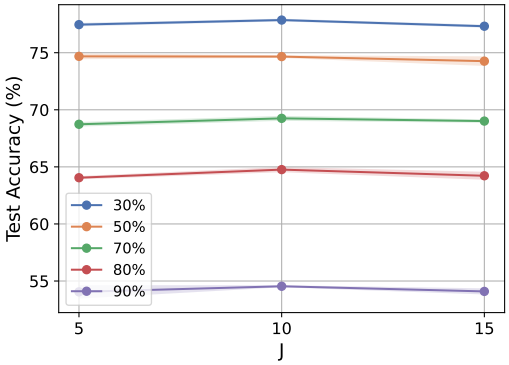

Figure 9: J varies from 5 to 15, showing minimal differences, which demonstrates its robustness. We fix $T = 30$, $C_{\mathcal{D}} = 4$. Runs are averaged over three runs.

B.1 Image Classification with Label Noise

We evaluated the robustness of our DUAL pruning method against label noise. We introduced symmetric label noise by replacing the original labels with labels from other classes randomly. For example, if we apply 20% label noise to a dataset with 100 classes, 20% of the data points are randomly selected, and each label is randomly reassigned to another label with a probability of $1/99$ for the selected data points.

Even under 30% and 40% random label noise, our method achieves the best performance and accurately identifies the noisy labels, as can be seen in Figure 10. By examining the proportion of noise removed, we can see that our method operates close to optimal.

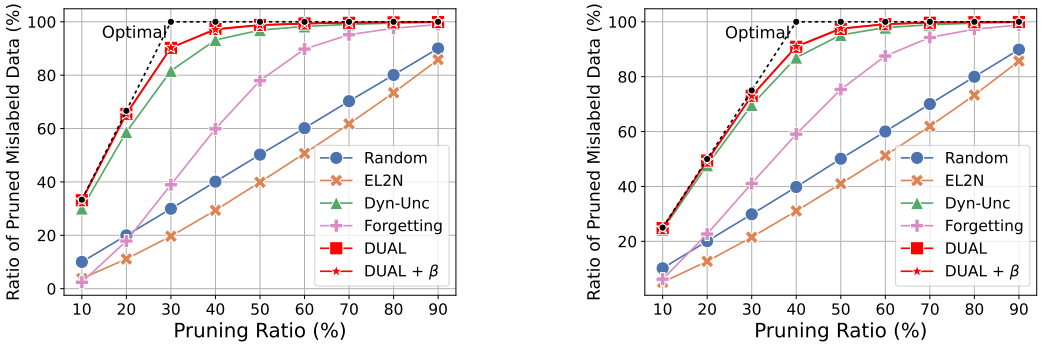

(a) 30% label noise

(b) 40% label noise

Figure 10: Ratio of pruned mislabeled data under 30% and 40% label noise on CIFAR-100

Figure 11 shows a scatter plot of the CIFAR-100 dataset under 20% label noise. The model is trained for 30 epochs, and we compute the prediction mean (y-axis) and standard deviation (x-axis) for each data point. Red dots represent the 20% mislabeled data. These points remain close to the origin (0,0) during the early training phase. Therefore, pruning at this stage allows us to remove mislabeled samples nearly optimally while selecting the most uncertain ones.

We evaluated the performance of our proposed method across a wide range of pruning levels, from 10% to 90%, and compared the final accuracy with that of baseline methods. As shown in the Table 5-8, our method consistently outperforms the competition with a substantial margin in most cases. For a comprehensive analysis of performance under noisy conditions, please refer to Tables 5 to 7 for CIFAR-100, which show results for 20%, 30%, and 40% noise, respectively. Additionally, the results for 20% label noise in Tiny-ImageNet are shown in Table 8.

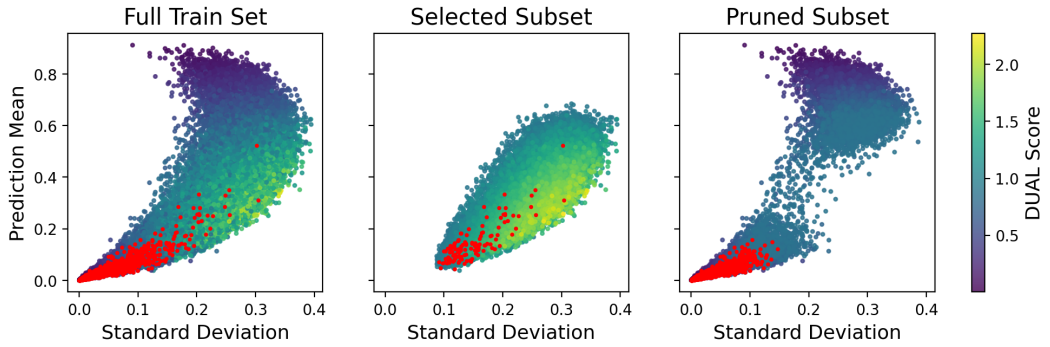

Figure 11: Pruning ratio is set to 50%. Only 116 data points over 10,000 mislabeled data are selected as a subset where red dots indicate mislabeled data.

Table 5: Comparison of test accuracy of DUAL pruning with existing coreset selection methods under 20% label noise using ResNet-18 for CIFAR-100. The model trained with the full dataset achieves **65.28%** test accuracy on average. Results are averaged over five runs.

Pruning Rate (→)	**10%**	**20%**	**30%**	**50%**	**70%**	**80%**	**90%**
Random	64.22 ±0.37	63.12 ±0.26	61.75 ±0.24	58.13 ±0.22	50.11 ±0.75	44.29 ±1.2	32.04 ±0.93
Entropy	63.51 ±0.25	60.59 ±0.23	56.75 ±0.37	44.90 ±0.74	24.43 ±0.12	16.60 ±0.29	10.35 ±0.49
Forgetting	64.29 ±0.26	63.40 ±0.14	64.00 ±0.27	67.51 ±0.52	59.29 ±0.66	50.11 ±0.91	32.08 ±1.15
EL2N	64.51 ±0.35	62.67 ±0.28	59.85 ±0.31	46.94 ±0.75	19.32 ±0.87	11.02 ±0.45	6.83 ±0.21
AUM	64.54 ±0.23	60.72 ±0.22	50.38 ±0.66	22.03 ±0.92	5.55 ±0.26	3.00 ±0.18	1.68 ±0.10
Moderate	64.45 ±0.29	62.90 ±0.33	61.46 ±0.50	57.53 ±0.61	49.50 ±1.06	43.81 ±0.80	29.15 ±0.79
Dyn-Unc	68.17 ±0.26	71.56 ±0.27	74.12 ±0.15	**73.43** ±0.12	67.21 ±0.27	61.38 ±0.27	48.00 ±0.79
TDDS	62.86 ±0.36	61.96 ±1.03	61.38 ±0.53	59.16 ±0.94	48.93 ±1.68	43.83 ±1.13	34.05 ±0.49
CCS	64.30 ±0.21	63.24 ±0.24	61.91 ±0.45	58.24 ±0.29	50.24 ±0.39	43.76 ±1.07	30.67 ±0.96
DUAL	69.78 ±0.28	**74.79** ±0.07	**75.40** ±0.11	**73.43** ±0.16	67.57 ±0.18	61.46 ±0.45	43.30 ±1.59
DUAL+β sampling	**69.95** ±0.60	74.68 ±1.22	75.37 ±1.33	73.29 ±0.84	**68.43** ±0.77	**63.74** ±0.35	**54.04** ±0.92

Table 6: Comparison of test accuracy of DUAL pruning with existing coreset selection methods under 30% label noise using ResNet-18 for CIFAR-100. The model trained with the full dataset achieves **58.25%** test accuracy on average. Results are averaged over five runs.

Pruning Rate (→)	**10%**	**20%**	**30%**	**50%**	**70%**	**80%**	**90%**
Random	57.67 ±0.52	56.29 ±0.55	54.70 ±0.60	51.41 ±0.38	42.67 ±0.80	36.86 ±1.01	25.64 ±0.82
Entropy	55.51 ±0.42	51.87 ±0.36	47.16 ±0.58	35.35 ±0.49	18.69 ±0.76	13.61 ±0.42	8.58 ±0.49
Forgetting	56.76 ±0.62	56.43 ±0.28	58.84 ±0.26	64.51 ±0.37	61.26 ±0.69	52.94 ±0.68	34.99 ±1.16
EL2N	56.39 ±0.53	54.41 ±0.68	50.29 ±0.40	35.65 ±0.79	13.05 ±0.51	8.52 ±0.40	6.16 ±0.40
AUM	56.51 ±0.56	49.10 ±0.72	37.57 ±0.66	11.56 ±0.46	2.79 ±0.23	1.87 ±0.24	1.43 ±0.12
Moderate	57.31 ±0.75	56.11 ±0.45	54.52 ±0.48	50.71 ±0.42	42.47 ±0.29	36.21 ±1.09	24.85 ±1.72
Dyn-Unc	62.20 ±0.44	66.48 ±0.40	70.45 ±0.50	**71.91** ±0.34	66.53 ±0.19	61.95 ±0.46	49.51 ±0.52
TDDS	57.24 ±0.44	55.64 ±0.46	53.97 ±0.46	49.04 ±1.05	39.90 ±1.21	35.02 ±1.34	26.99 ±1.03
CCS	57.26 ±0.48	56.52 ±0.23	54.76 ±0.52	51.29 ±0.32	42.33 ±0.78	36.61 ±1.31	25.64 ±1.65
DUAL	62.42 ±0.48	**67.52** ±0.40	**72.65** ±0.17	71.55 ±0.23	66.35 ±0.14	61.57 ±0.44	48.70 ±0.19
DUAL+β sampling	**63.02** ±0.41	**67.52** ±0.24	72.57 ±0.15	71.68 ±0.27	**66.75** ±0.45	**62.28** ±0.43	**52.60** ±0.87

Table 7: Comparison of test accuracy of DUAL pruning with existing coreset selection methods under 40% label noise using ResNet-18 for CIFAR-100. The model trained with the full dataset achieves **52.74%** test accuracy on average. Results are averaged over five runs.

Pruning Rate (→)	**10%**	**20%**	**30%**	**50%**	**70%**	**80%**	**90%**
Random	51.13 ±0.71	48.42 ±0.46	46.99 ±0.29	43.24 ±0.46	33.60 ±0.50	28.28 ±0.81	19.52 ±0.79
Entropy	49.14 ±0.32	46.06 ±0.58	41.83 ±0.73	28.26 ±0.37	15.64 ±0.19	12.21 ±0.68	8.23 ±0.40
Forgetting	50.98 ±0.72	50.36 ±0.48	52.86 ±0.47	60.48 ±0.68	61.55 ±0.58	54.57 ±0.86	37.68 ±1.63
EL2N	50.09 ±0.86	46.35 ±0.48	41.57 ±0.26	23.42 ±0.80	9.00 ±0.25	6.80 ±0.44	5.58 ±0.40
AUM	50.60 ±0.54	41.84 ±0.76	26.29 ±0.72	5.49 ±0.19	1.95 ±0.21	1.44 ±0.14	1.43 ±0.24
Moderate	50.62 ±0.27	48.70 ±0.79	47.01 ±0.21	42.73 ±0.39	32.35 ±1.29	27.72 ±1.69	19.85 ±1.11
Dyn-Unc	54.46 ±0.27	59.02 ±0.23	63.86 ±0.47	69.76 ±0.16	**65.36** ±0.14	61.37 ±0.32	50.49 ±0.71
TDDS	50.65 ±0.23	48.83 ±0.38	46.93 ±0.66	41.85 ±0.37	33.31 ±0.79	29.39 ±0.35	21.09 ±0.89
CCS	64.30 ±0.29	48.54 ±0.35	46.81 ±0.45	42.57 ±0.32	33.19 ±0.88	28.32 ±0.59	19.61 ±0.75
DUAL	54.46 ±0.33	58.99 ±0.34	**64.71** ±0.44	69.87 ±0.28	64.21 ±0.21	59.90 ±0.44	49.61 ±0.27
DUAL+β sampling	**54.53** ±0.06	**59.65** ±0.41	64.67 ±0.34	**70.09** ±0.33	65.12 ±0.46	60.62 ±0.30	**51.51** ±0.41

Table 8: Comparison of test accuracy of DUAL pruning with existing coreset selection methods under 20% label noise using ResNet-34 for Tiny-ImageNet. The model trained with the full dataset achieves **42.24%** test accuracy on average. Results are averaged over three runs.

Pruning Rate (→)	**10%**	**20%**	**30%**	**50%**	**70%**	**80%**	**90%**
Random	41.09 ±0.29	39.24 ±0.39	37.17 ±0.23	32.93 ±0.45	26.12 ±0.63	22.11 ±0.42	13.88 ±0.60
Entropy	40.69 ±0.06	38.14 ±0.92	35.93 ±1.56	31.24 ±1.76	23.65 ±2.05	18.53 ±2.10	10.52 ±1.64
Forgetting	43.60 ±0.65	44.82 ±0.20	45.65 ±0.48	46.05 ±0.07	41.08 ±0.53	34.89 ±0.12	24.58 ±0.06
EL2N	41.05 ±0.35	38.88 ±0.63	32.91 ±0.39	20.89 ±0.80	8.08 ±0.24	4.92 ±0.32	3.12 ±0.07
AUM	40.20 ±0.27	34.68 ±0.35	29.01 ±0.12	10.45 ±0.85	2.52 ±0.75	1.30 ±0.23	0.79 ±0.40
Moderate	41.23 ±0.38	38.58 ±0.60	37.60 ±0.66	32.65 ±1.18	25.68 ±0.40	21.74 ±0.63	14.15 ±0.73
Dyn-Unc	45.67 ±0.78	47.49 ±0.46	49.38 ±0.17	47.47 ±0.32	42.49 ±0.39	37.44 ±0.73	28.48 ±0.73
TDDS	36.56 ±0.54	36.90 ±0.48	47.62 ±1.36	42.44 ±0.63	34.32 ±0.26	24.32 ±0.26	17.43 ±0.17
CCS	40.49 ±0.67	39.06 ±0.24	37.67 ±0.46	30.83 ±1.02	22.38 ±0.70	19.66 ±0.58	12.23 ±0.64
DUAL	**45.76** ±0.67	**48.20** ±0.20	**49.94** ±0.17	**48.19** ±0.27	42.80 ±0.74	**37.90** ±0.59	27.80 ±0.49
DUAL+β sampling	45.21 ±0.08	47.76 ±0.33	48.99 ±0.32	46.95 ±0.23	**43.01** ±0.43	**37.91** ±0.28	**28.78** ±0.57

B.2 Image Classification with Image Corruption

We also evaluated the robustness of our proposed method against five different types of realistic image corruption: motion blur, fog, reduced resolution, rectangular occlusion, and Gaussian noise across the corruption rate from 20% to 40%. The ratio of each type of corruption is 4% for 20% corruption, 6% for 30% corruption, and 8% for 40% corruption. Example images for each type of corruption can be found in Figure 12. Motion blur, reduced resolution, and rectangular occlusion are somewhat distinguishable, whereas fog and Gaussian noise are difficult for the human eye to differentiate. Somewhat surprisingly, our DUAL pruning prioritizes removing the most challenging examples, such as fog and Gaussian corrupted images, as shown in Figure 14.

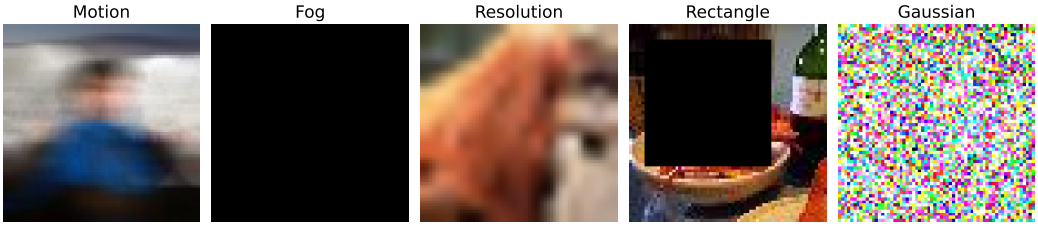

Figure 12: Examples of the different types of noise used for image corruption. Here we consider motion blur, fog, resolution, rectangle, and Gaussian noise.

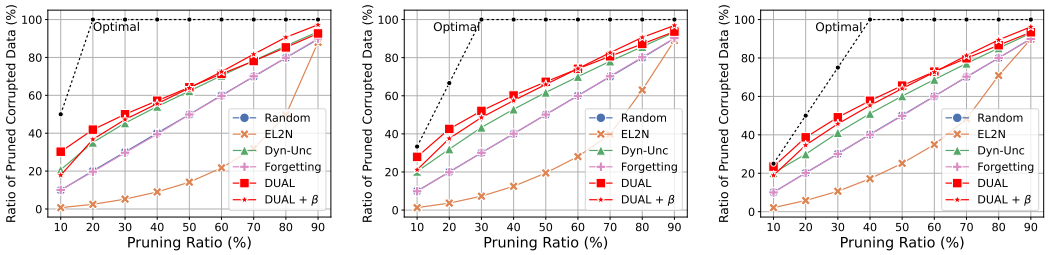

(a) 20% image corruption (b) 30% image corruption (c) 40% image corruption

Figure 13: Ratio of pruned corrupted samples with corruption rate of 20%, 30% and 40% on CIFAR-100.

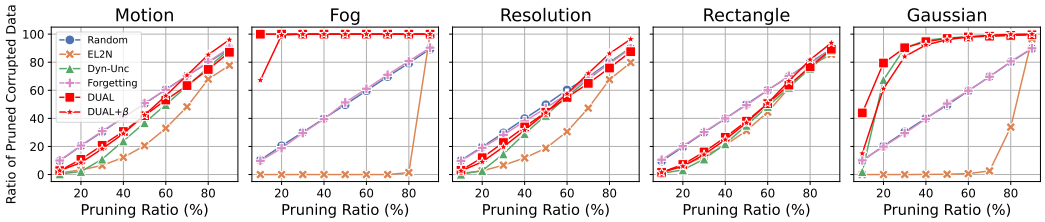

Figure 14: Illustration of the different types of noise used for image corruption. DUAL pruning prioritizes removing the most challenging corrupted images, such as fog and Gaussian noise.

We evaluated the performance of our proposed method across a wide range of pruning levels, from 10% to 90%, and compared the final accuracy with that of baseline methods. As shown in the table, our method consistently outperforms the competitors in most cases. For a comprehensive analysis of performance under noisy conditions, please refer to Tables 9 to 11 for CIFAR-100, which show results for 20%, 30%, and 40% corrupted images, respectively. Additionally, the results for 20% image corruption in Tiny-ImageNet are shown in Table 12.

Table 9: Comparison of test accuracy of DUAL pruning with existing coreset selection methods under 20% image corrupted data using ResNet-18 for CIFAR-100. The model trained with the full dataset achieves **75.45%** test accuracy on average. Results are averaged over five runs.

Pruning Rate (→)	**10%**	**20%**	**30%**	**50%**	**70%**	**80%**	**90%**
Random	74.54 ±0.14	73.08 ±0.27	71.61 ±0.14	67.52 ±0.32	59.57 ±0.52	52.79 ±0.68	38.26 ±1.32
Entropy	74.74 ±0.25	73.15 ±0.26	71.15 ±0.13	64.97 ±0.52	49.49 ±1.40	35.92 ±0.64	17.91 ±0.45
Forgetting	74.33 ±0.25	73.25 ±0.29	71.68 ±0.37	67.31 ±0.23	58.93 ±0.35	52.01 ±0.62	38.95 ±1.24
EL2N	75.22 ±0.09	74.23 ±0.11	72.01 ±0.18	48.19 ±0.47	14.81 ±0.14	8.68 ±0.06	7.60 ±0.18
AUM	75.26 ±0.25	74.47 ±0.31	71.96 ±0.22	47.50 ±1.39	15.35 ±1.79	8.98 ±1.37	5.47 ±0.85
Moderate	75.25 ±0.23	74.34 ±0.31	72.80 ±0.25	68.75 ±0.40	60.98 ±0.39	54.21 ±0.93	38.72 ±0.30
Dyn-Unc	75.22 ±0.25	75.51 ±0.22	75.09 ±0.23	72.02 ±0.07	62.17 ±0.55	53.49 ±0.47	35.44 ±0.49
TDDS	73.29 ±0.40	72.90 ±0.31	71.83 ±0.78	67.24 ±0.92	57.30 ±3.11	55.14 ±1.21	41.58 ±2.10
CCS	74.31 ±0.14	73.04 ±0.23	71.83 ±0.25	67.61 ±0.48	59.61 ±0.64	53.35 ±0.71	39.04 ±1.14
DUAL	**75.95** ±0.19	75.66 ±0.23	**75.10** ±0.23	**72.64** ±0.27	65.29 ±0.64	57.55 ±0.55	37.34 ±1.70
DUAL+β sampling	75.50 ±0.21	**75.78** ±0.15	**75.10** ±0.13	72.08 ±0.22	**65.84** ±0.37	**62.20** ±0.72	**53.96** ±0.35

Table 10: Comparison of test accuracy of DUAL pruning with existing coreset selection methods under 30% image corrupted data using ResNet-18 for CIFAR-100. The model trained with the full dataset achieves **73.77%** test accuracy on average. Results are averaged over five runs.

Pruning Rate (→)	**10%**	**20%**	**30%**	**50%**	**70%**	**80%**	**90%**
Random	72.71 ±0.34	71.28 ±0.31	69.84 ±0.24	65.42 ±0.33	56.72 ±0.56	49.71 ±0.65	35.75 ±1.41
Entropy	72.94 ±0.09	71.14 ±0.14	68.74 ±0.20	61.34 ±0.59	42.70 ±1.02	29.46 ±1.68	12.55 ±0.66
Forgetting	72.67 ±0.21	71.22 ±0.08	69.65 ±0.45	65.25 ±0.33	56.47 ±0.31	49.07 ±0.32	34.62 ±1.15
EL2N	73.33 ±0.08	71.99 ±0.11	67.72 ±0.50	37.57 ±0.70	10.75 ±0.28	9.08 ±0.30	7.75 ±0.08
AUM	73.73 ±0.19	72.99 ±0.22	70.93 ±0.33	57.13 ±0.42	28.98 ±0.50	19.73 ±0.28	12.18 ±0.46
Moderate	**74.02** ±0.28	72.70 ±0.30	71.51 ±0.26	67.35 ±0.16	59.47 ±0.34	52.95 ±0.60	37.45 ±1.21
Dyn-Unc	73.86 ±0.21	73.78 ±0.20	**73.78** ±0.12	71.01 ±0.23	61.56 ±0.46	52.51 ±1.08	35.47 ±1.34
TDDS	71.58 ±0.50	71.45 ±0.68	69.92 ±0.25	65.12 ±2.08	55.79 ±2.16	53.85 ±0.94	40.51 ±1.34
CCS	72.58 ±0.12	71.38 ±0.35	69.83 ±0.26	65.45 ±0.23	56.65 ±0.45	49.75 ±0.90	34.63 ±1.79
DUAL	73.96 ±0.20	**74.07** ±0.43	73.74 ±0.18	**71.23** ±0.08	64.76 ±0.32	57.47 ±0.51	37.93 ±2.38
DUAL+β sampling	73.91 ±0.17	73.80 ±0.48	73.59 ±0.19	71.12 ±0.29	**65.18** ±0.44	**61.07** ±0.47	**52.61** ±0.47

Table 11: Comparison of test accuracy of DUAL pruning with existing coreset selection methods under 40% image corrupted data using ResNet-18 for CIFAR-100. The model trained with the full dataset achieves **72.16%** test accuracy on average. Results are averaged over five runs.

Pruning Rate (→)	**10%**	**20%**	**30%**	**50%**	**70%**	**80%**	**90%**
Random	70.78 ±0.25	69.30 ±0.29	67.98 ±0.26	63.23 ±0.26	53.29 ±0.64	45.76 ±0.85	32.63 ±0.61
Entropy	70.74 ±0.18	68.90 ±0.37	66.19 ±0.46	57.03 ±0.60	35.62 ±1.58	22.50 ±1.03	7.46 ±0.52
Forgetting	70.54 ±0.10	69.17 ±0.30	67.41 ±0.28	62.77 ±0.15	52.89 ±0.36	44.94 ±0.66	30.48 ±0.49
EL2N	71.57 ±0.28	69.24 ±0.16	62.95 ±0.52	28.33 ±0.47	9.48 ±0.21	8.86 ±0.21	7.58 ±0.16
AUM	71.66 ±0.23	69.75 ±0.30	62.10 ±0.46	26.56 ±0.62	8.93 ±0.19	5.82 ±0.09	4.15 ±0.11
Moderate	**72.10** ±0.14	71.55 ±0.25	69.84 ±0.39	65.74 ±0.21	56.96 ±0.52	49.04 ±0.74	34.87 ±0.57
Dyn-Unc	71.86 ±0.12	71.65 ±0.18	**71.79** ±0.27	69.17 ±0.44	59.69 ±0.30	51.36 ±0.70	34.02 ±0.45
TDDS	70.02 ±0.43	69.27 ±0.74	68.03 ±0.55	63.42 ±0.77	55.28 ±1.93	51.44 ±1.36	38.42 ±0.80
CCS	70.84 ±0.41	69.08 ±0.41	68.11 ±0.09	63.36 ±0.16	53.21 ±0.54	46.27 ±0.52	32.72 ±0.52
DUAL	71.90 ±0.27	**72.38** ±0.27	**71.79** ±0.11	**69.69** ±0.18	63.35 ±0.29	56.57 ±1.07	37.78 ±0.73
DUAL+β sampling	71.96 ±0.13	71.92 ±0.22	71.69 ±0.18	69.23 ±0.15	**63.73** ±0.43	**59.75** ±0.32	**51.51** ±0.68

Table 12: Comparison of test accuracy of DUAL pruning with existing coreset selection methods under 20% image corrupted data using ResNet-34 for Tiny-ImageNet. The model trained with the full dataset achieves **57.12%** test accuracy on average. Results are averaged over three runs.

Pruning Rate ($\rightarrow$)	**10%**	**20%**	**30%**	**50%**	**70%**	**80%**	**90%**
Random	49.59 ±0.93	48.64 ±0.94	45.64 ±0.53	41.58 ±0.66	33.98 ±0.55	28.88 ±0.67	18.59 ±0.25
Entropy	50.34 ±0.19	48.02 ±0.49	44.80 ±0.30	36.58 ±0.19	25.20 ±0.53	16.55 ±0.40	3.32 ±0.26
Forgetting	46.81 ±0.26	41.16 ±0.28	35.58 ±0.17	26.80 ±0.18	17.66 ±0.23	12.61 ±0.04	6.01 ±0.19
EL2N	50.66 ±0.27	47.76 ±0.25	42.15 ±1.02	23.42 ±0.26	8.07 ±0.09	6.57 ±0.36	3.75 ±0.13
AUM	51.11 ±0.73	47.70 ±0.51	42.04 ±0.81	20.85 ±0.79	6.87 ±0.24	3.75 ±0.21	2.27 ±0.11
Moderate	51.43 ±0.76	49.85 ±0.23	47.85 ±0.31	42.31 ±0.40	35.00 ±0.49	29.63 ±0.67	19.51 ±0.72
Dyn-Unc	51.61 ±0.19	51.47 ±0.34	**51.18** ±0.58	**48.88** ±0.85	42.52 ±0.34	37.85 ±0.47	26.26 ±0.70
TDDS	51.53 ±0.40	49.81 ±0.21	48.98 ±0.27	45.81 ±0.16	38.05 ±0.70	33.04 ±0.39	22.66 ±1.28
CCS	50.26 ±0.78	48.00 ±0.41	45.38 ±0.63	40.98 ±0.23	33.49 ±0.04	27.18 ±0.66	15.37 ±0.54
DUAL	51.22 ±0.40	**52.06** ±0.55	50.88 ±0.64	47.03 ±0.56	40.03 ±0.09	34.92 ±0.15	20.41 ±1.07
DUAL+β sampling	**52.15** ±0.25	51.11 ±0.34	50.21 ±0.36	46.85 ±0.27	**42.97** ±0.28	**38.30** ±0.06	**27.45** ±0.50

B.3 CROSS-ARCHITECTURE GENERALIZATION

In this section, we investigate the cross-architecture generalization ability of our proposed method. Specifically, we calculate the example score on one architecture and test its coreset performance on a different architecture. This evaluation aims to assess the ability of example scores to be transferred across diverse architectural designs.

Table 13: Cross-architecture generalization performance on CIFAR-100 from three layer CNN to ResNet-18. We report an average of five runs. 'R18 → R18' stands for score computation on ResNet-18, as a baseline.

	3-layer CNN → ResNet-18			
Pruning Rate (→)	30%	50%	70%	90%
Random	75.15 ±0.28	71.68 ±0.31	64.86 ±0.39	45.09 ±1.26
EL2N	76.56 ±0.65	71.78 ±0.32	56.57 ±1.32	22.84 ±3.54
Dyn-Unc	**76.61** ±0.75	72.92 ±0.57	65.97 ±0.53	44.25 ±2.47
CCS	75.29 ±0.20	72.06 ±0.19	**66.11** ±0.15	36.98 ±1.47
DUAL	**76.61** ±0.08	**73.55** ±0.12	65.97 ±0.18	39.00 ±2.51
DUAL+β sampling	76.36 ±0.18	72.46 ±0.41	65.50 ±0.53	**48.91** ±0.60
DUAL (R18→R18)	77.43 ±0.18	74.62 ±0.47	66.41 ±0.52	34.38 ±1.39
DUAL (R18→R18) +β sampling	77.86 ±0.12	74.66 ±0.12	69.25 ±0.22	54.54 ±0.09

Table 14: Cross-architecture generalization performance on CIFAR-100 from three layer CNN to VGG-16. We report an average of five runs. 'V16 → V16' stands for score computation on VGG-16, as a baseline.

	3-layer CNN → VGG-16			
Pruning Rate (→)	30%	50%	70%	90%
Random	69.47 ±0.27	65.52 ±0.54	57.18 ±0.68	34.69 ±1.97
EL2N	70.35 ±0.64	63.66 ±1.49	46.12 ±6.87	20.85 ±9.03
Dyn-Unc	71.18 ±0.96	67.06 ±0.94	58.87 ±0.83	31.57 ±3.29
CCS	69.56 ±0.33	65.26 ±0.50	57.60 ±0.80	23.92 ±1.85
DUAL	**71.75** ±0.16	**67.91** ±0.27	59.08 ±0.64	29.16 ±2.28
DUAL+β sampling	70.78 ±0.41	67.47 ±0.44	**60.33** ±0.32	**43.92** ±1.15
DUAL (V16→V16)	73.63 ±0.62	69.66 ±0.45	58.49 ±0.77	32.96 ±1.12
DUAL (V16→V16) +β sampling	72.77 ±0.41	68.93 ±0.23	61.48 ±0.36	42.99±0.62

Table 15: Cross-architecture generalization performance on CIFAR-100 from VGG-16 to ResNet-18. We report an average of five runs. 'R18 → R18' stands for score computation on ResNet-18, as a baseline.

	VGG-16 → ResNet-18			
Pruning Rate (→)	30%	50%	70%	90%
Random	75.15 ±0.28	71.68 ±0.31	64.86 ±0.39	45.09 ±1.26
EL2N	76.42 ±0.27	70.44 ±0.48	51.87 ±1.27	25.74 ±1.53
Dyn-Unc	**77.59** ±0.19	74.20 ±0.22	65.24 ±0.36	42.95 ±1.14
CCS	75.19 ±0.19	71.56 ±0.28	64.83 ±0.25	**46.08** ±1.23
DUAL	77.40 ±0.36	**74.29** ±0.12	63.74 ±0.30	36.87 ±2.27
DUAL+ β sampling	76.67 ±0.15	73.14 ±0.29	**65.69** ±0.57	45.95 ±0.52
DUAL (R18→R18)	77.43 ±0.18	74.62 ±0.47	66.41 ±0.52	34.38 ±1.39
DUAL (R18→R18) +β sampling	77.86 ±0.12	74.66 ±0.12	69.25 ±0.22	54.54 ±0.09

Table 16: Cross-architecture generalization performance on CIFAR-100 from ResNet-18 to VGG-16. We report an average of five runs. 'V16 → V16' stands for score computation on VGG-16, as a baseline.

	ResNet-18 → VGG-16			
Pruning Rate (→)	30%	50%	70%	90%
Random	70.99 ±0.33	67.34 ±0.21	60.18 ±0.52	41.69 ±0.72
EL2N	72.43 ±0.54	65.36 ±0.68	43.35 ±0.81	19.92 ±0.89
Dyn-Unc	73.34 ±0.29	69.24 ±0.39	57.67 ±0.52	31.74 ±0.80
CCS	71.18 ±0.16	67.35 ±0.38	59.77 ±0.43	41.06 ±1.03
DUAL	73.44 ±0.29	69.87 ±0.35	60.07 ±0.47	29.74 ±1.70
DUAL +β sampling	**73.50** ±0.27	**70.43** ±0.26	**64.48** ±0.47	**49.61** ±0.49
DUAL (V16→V16)	73.63 ±0.61	69.66 ±0.45	58.49 ±0.77	32.96 ±1.12
DUAL (V16→V16)+β sampling	72.66 ±0.17	68.80 ±0.34	60.40 ±0.68	41.51 ±0.47

Table 17: Cross-architecture generalization performance on CIFAR-100 from ResNet-18 to ResNet-50. We report an average of five runs. 'R50 → R50' stands for score computation on ResNet-50, as a baseline.

	ResNet-18 → ResNet-50			
Pruning Rate (→)	30%	50%	70%	90%
Random	74.47 ±0.67	70.09 ±0.42	60.06 ±0.99	41.91 ±4.32
EL2N	76.42 ±1.00	69.14 ±1.00	45.16 ±3.21	19.63 ±1.15
Dyn-Unc	77.31 ±0.34	72.12 ±0.68	59.38 ±2.35	31.74 ±2.31
CCS	74.78 ±0.66	69.98 ±1.18	59.75 ±1.41	41.54 ±3.94
DUAL	**78.03** ±0.83	72.82 ±1.46	63.08 ±2.45	33.65 ±2.92
DUAL +β sampling	77.82 ±0.65	**73.98** ±0.62	**66.36** ±1.66	**49.90** ±2.56
DUAL (R50→R50)	77.82 ±0.64	73.66 ±0.85	52.12 ±2.73	26.13 ±1.96
DUAL (R50→R50)+β sampling	77.57 ±0.23	73.44 ±0.87	65.17 ±0.96	47.63 ±2.47

Table 18: Cross-architecture generalization performance on CIFAR-100 from VGG-16 to ResNet-50. We report an average of five runs. 'R50 → R50' stands for score computation on ResNet-50, as a baseline

	VGG-16 → ResNet-50			
Pruning Rate (→)	30%	50%	70%	90%
Random	71.13 ±6.52	70.31 ±1.20	61.02 ±1.68	41.03 ±3.74
EL2N	76.30 ±0.69	67.11 ±3.09	44.88 ±3.65	25.05 ±1.76
Dyn-Unc	**77.91** ±0.54	**73.52** ±0.41	62.37 ±0.62	39.10 ±4.04
CCS	75.40 ±0.64	70.44 ±0.49	60.10 ±1.24	41.94 ±3.01
DUAL	77.50 ±0.53	71.81 ±0.48	60.68 ±1.67	34.88 ±3.47
DUAL +β sampling	76.67 ±0.15	73.14 ±0.29	**65.69** ±0.57	**45.95** ±0.52
DUAL (R50→R50)	77.82 ±0.64	73.66 ±0.85	52.12 ±2.73	26.13 ±1.96
DUAL (R50→R50)+β sampling	77.57 ±0.23	73.44 ±0.87	65.17 ±0.96	47.63 ±2.47

B.4 Effectiveness of Beta Sampling

We study the impact of our Beta sampling on existing score metrics. We apply our Beta sampling strategy to forgetting, EL2N, and Dyn-Unc scores of CIFAR10 and 100. By comparing Beta sampling with the vanilla threshold pruning using scores, we observe that prior score-based methods become competitive, outperforming random pruning when Beta sampling is adjusted.

Table 19: Comparison on CIFAR-10 and CIFAR-100 for 90% pruning rate. We report average accuracy with five runs. The best performance is in bold in each column.

	CIFAR-10		CIFAR-100	
Method	Thresholding	β-Sampling	Thresholding	β-Sampling
Random	**83.74** ± 0.21	83.31 (-0.43) ± 0.14	45.09 ± 1.26	51.76 (+6.67) ± 0.25
EL2N	38.74 ± 0.75	87.00 (+48.26) ± 0.45	8.89 ± 0.28	53.97 (+45.08) ± 0.63
Forgetting	46.64 ± 1.90	85.67 (+39.03) ±0.13	26.87 ± 0.73	52.40 (+25.53) ± 0.43
Dyn-Unc	59.67 ± 1.79	85.33 (+32.14) ± 0.20	34.57 ± 0.69	51.85 (+17.28) ± 0.35
DUAL	54.95 ± 0.42	**87.09** (+31.51) ± 0.36	34.28 ± 1.39	**54.54** (+20.26) ± 0.09

Table 20: Comparison on CIFAR-10 and CIFAR-100 for 80% pruning rate. We report average accuracy with five runs. The best performance is in bold in each column.

	CIFAR-10		CIFAR-100	
Method	Thresholding	β-Sampling	Thresholding	β-Sampling
Random	**88.28** ± 0.17	88.83 (+0.55) ± 0.18	**59.23** ± 0.62	61.74 (+2.51) ± 0.15
EL2N	74.70 ± 0.45	87.69 (+12.99) ± 0.98	19.52 ± 0.79	63.98 (+44.46) ± 0.73
Forgetting	75.47 ± 1.27	90.86 (+15.39) ± 0.07	39.09 ± 0.41	63.29 (+24.20) ± 0.13
Dyn-Unc	83.32 ± 0.94	90.80 (+7.48) ± 0.30	55.01 ± 0.55	62.31 (+7.30) ± 0.23
DUAL	82.02 ± 1.85	**91.42** (+9.68) ± 0.35	56.57 ± 0.57	**64.76** (+8.46) ± 0.23

We also study the impact of our pruning strategy with DUAL score combined with Beta sampling. We compare different sampling strategies $i.e.$ vanilla thresholding, stratified sampling Zheng et al. (2022), and our proposed Beta sampling on CIFAR10 and 100, at 80% and 90% pruning rates. We observe that our proposed method mostly performs the best, especially with the high pruning ratio.

Table 21: Comparison on Sampling Strategy

CIFAR10					
Pruning Rate	30%	50%	70%	80%	90%
DUAL	95.35	95.08	91.95	81.74	55.58
DUAL + CCS	**95.54**	95.00	92.83	90.49	81.67
DUAL + β	95.51	**95.23**	**93.04**	**91.42**	**87.09**
CIFAR100					
Pruning Rate	30%	50%	70%	80%	90%
DUAL	77.61	**74.86**	66.39	56.50	34.28
DUAL + CCS	75.21	71.53	64.30	59.09	45.21
DUAL + β	**77.86**	74.66	**69.25**	**64.76**	**54.54**

C Detailed Explanation about Our Method

In this section, we provide details on the implementation used across all experiments for reproducibility. Appendix C.2 presents the full algorithm for our pruning method, DUAL, along with the Beta sampling strategy. Additionally, in a later subsection, we visualize the selected data using Beta sampling.

Recall that we define our sampling distribution $\mathrm{Beta}(\alpha_r, \beta_r)$ as follows:

$$\begin{aligned} \beta_r &= C\,(1-\mu_{\mathcal{D}})\,(1-r^{c_{\mathcal{D}}}) \\ \alpha_r &= C - \beta_r, \end{aligned} \tag{6}$$

where $\mu_{\mathcal{D}} \in [0, 1]$ is the probability mean of the highest DUAL score training sample. To ensure stability, we compute this as the average probability mean of the 10 highest DUAL score training samples. Additionally, as mentioned earlier, we set the value of C to 15 across all experiments. For technical details, we add 1 to α_r to further ensure that the PDF remains stationary at low pruning ratios.

We illustrate the Beta PDF, as defined above, in Figure 15 for different values of $c_{\mathcal{D}}$. In both subplots, we set $\mu_{\mathcal{D}}$ as 0.25. The left subplot shows the PDF with $c_{\mathcal{D}} = 5.5$, which corresponds to the value used in CIFAR-10 experiments, while the right subplot visualizes the PDF where $c_{\mathcal{D}} = 4$, corresponding to CIFAR-100.

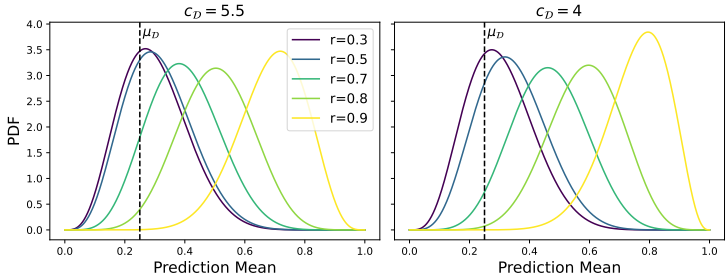

Figure 15: Visualization of Beta distribution for varying $c_{\mathcal{D}}$. The left subplot corresponds to the value used in CIFAR-10, and the right subplot corresponds to the value used in CIFAR-100.

C.1 Visualization of Selected Data with Beta Sampling

Here we illustrate the sampling probability of being selected into coreset, selected samples, and pruned samples in each figure when using the DUAL score combined with Beta sampling. As the pruning ratio increases, we focus on including easier samples.

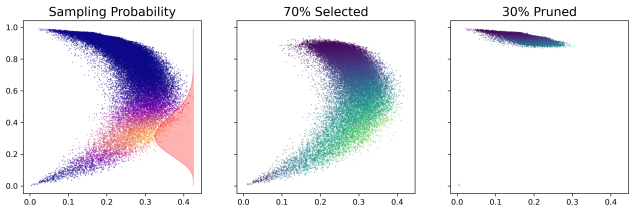

(a) CIFAR-100 at pruning ratio 30%

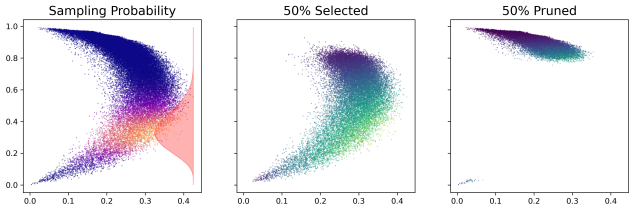

(b) CIFAR-100 at pruning ratio 50%

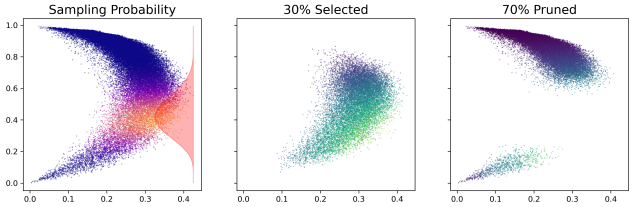

(c) CIFAR-100 at pruning ratio 70%

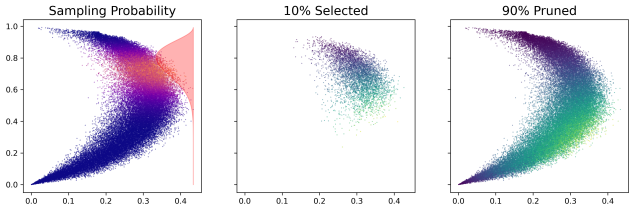

(d) CIFAR-100 at pruning ratio 90%

Figure 16: Pruning visualization on CIFAR-100.

C.2 Algorithm of Proposed Pruning Method

The detailed algorithms for DUAL pruning and Beta sampling are as follows:

Algorithm 1 DUAL pruning + β-sampling

input Training dataset $\mathcal{D}$, pruning ratio r, dataset simplicity $c_{\mathcal{D}}$, training epoch T, window length J.
output Subset $\mathcal{S} \subset \mathcal{D}$ such that $|\mathcal{S}| = (1-r)|\mathcal{D}|$
  for $(\boldsymbol{x}_i, y_i) \in \mathcal{D}$ **do**
    for $k = 1, \cdots, T-J+1$ **do**
      $\bar{\mathbb{P}}_k(\boldsymbol{x}_i, y_i) \leftarrow \frac{1}{J}\sum_{j=0}^{J-1} \mathbb{P}_{k+j}(y_i \mid \boldsymbol{x}_i)$
      $\mathbb{U}_k(\boldsymbol{x}_i, y_i) \leftarrow \sqrt{\frac{1}{J-1}\sum_{j=0}^{J-1}\left[\mathbb{P}_{k+j}(y_i \mid \boldsymbol{x}_i) - \bar{\mathbb{P}}_k(\boldsymbol{x}_i, y_i)\right]^2}$
      $\mathrm{DUAL}_k(\boldsymbol{x}_i, y_i) \leftarrow (1 - \bar{\mathbb{P}}_k(\boldsymbol{x}_i, y_i)) \times \mathbb{U}_k(\boldsymbol{x}_i, y_i)$
    end for
    $\mathrm{DUAL}(\boldsymbol{x}_i, y_i) \leftarrow \frac{1}{T-J+1}\sum_{k=1}^{T-J+1} \mathrm{DUAL}_k(\boldsymbol{x}_i, y_i)$
  end for
  if β-sampling **then**
    for $(\boldsymbol{x}_i, y_i) \in \mathcal{D}$ **do**
      $\bar{\mathbb{P}}(\boldsymbol{x}_i, y_i) \leftarrow \frac{1}{T}\sum_{k=1}^{T} \mathbb{P}_k(y_i \mid \boldsymbol{x}_i)$
      $\varphi\left(\bar{\mathbb{P}}(\boldsymbol{x}_i, y_i)\right) \leftarrow$ PDF value of $\mathrm{Beta}(\alpha_r, \beta_r)$ from Equation (5)
      $\tilde{\varphi}(\boldsymbol{x}_i) \leftarrow \varphi\left(\bar{\mathbb{P}}(\boldsymbol{x}_i, y_i)\right) \times \mathrm{DUAL}(\boldsymbol{x}_i, y_i)$
    end for
    $\tilde{\varphi}(\boldsymbol{x}_i) \leftarrow \frac{\tilde{\varphi}(\boldsymbol{x}_i)}{\sum_{j \in \mathcal{D}} \tilde{\varphi}(\boldsymbol{x}_j)}$
    $\mathcal{S} \leftarrow$ Sample $(1-r)|\mathcal{D}|$ data points according to $\tilde{\varphi}(\boldsymbol{x}_i)$
  else
    $\mathcal{S} \leftarrow$ Sample $(1-r)|\mathcal{D}|$ data points with the largest $\mathrm{DUAL}(\boldsymbol{x}_i, y_i)$ score
  end if

D THEORETICAL RESULTS

Throughout this section, we will rigorously prove Theorem 3.1, providing the intuition that Dyn-Unc takes longer than our method to select informative samples.

D.1 PROOF OF THEOREM 3.1

Assume that the input and output (or label) space are $\mathcal{X} = \mathbb{R}^n$ and $\mathcal{Y} = \{\pm 1\}$, respectively. Let the model $f : \mathcal{X} \to \mathbb{R}$ be of the form $f(\boldsymbol{x}; \boldsymbol{w}) = \boldsymbol{w}^\top \boldsymbol{x}$ parameterized by $\boldsymbol{w} \in \mathbb{R}^n$ with zero-initialization. Let the loss be the exponential loss, $\ell(z) = e^{-z}$. Exponential loss is reported to induce implicit bias similar to logistic loss in binary classification tasks using linearly separable datasets (Soudry et al., 2018; Gunasekar et al., 2018).

The task of the model is to learn a binary classification. The dataset $\mathcal{D}$ consists only two points, i.e. $\mathcal{D} = \{(\boldsymbol{x}_1, y_1^*), (\boldsymbol{x}_2, y_2^*)\}$, where without loss of generality $y_i^* = 1$ for $i = 1, 2$. The model learns from $\mathcal{D}$ with the gradient descent. The update rule, equipped with a learning rate $\eta > 0$, is:

$$\begin{aligned} \boldsymbol{w}_0 &= 0 \\ \boldsymbol{w}_{t+1} &= \boldsymbol{w}_t - \eta \nabla_{\boldsymbol{w}} \left[\sum_{i=1}^{2} \ell\left(f\left(\boldsymbol{x}_i; \boldsymbol{w}_t\right)\right) \right] \\ &= \boldsymbol{w}_t + \eta \left(e^{-\boldsymbol{w}_t^\top \boldsymbol{x}_1} \boldsymbol{x}_1 + e^{-\boldsymbol{w}_t^\top \boldsymbol{x}_2} \boldsymbol{x}_2 \right). \end{aligned}$$

For brevity, denote the model output of the i-th data point at the t-th epoch as $y_t^{(i)} := f(\boldsymbol{x}_i; \boldsymbol{w}_t)$. The update rule for the parameter is simplified as:

$$\boldsymbol{w}_{t+1} = \boldsymbol{w}_t + \eta \left(e^{-y_t^{(1)}} \boldsymbol{x}_1 + e^{-y_t^{(2)}} \boldsymbol{x}_2 \right). \tag{7}$$

We also derive the update rule of model output for each instance:

$$\begin{cases} y_{t+1}^{(1)} = \boldsymbol{w}_{t+1}^\top \boldsymbol{x}_1 = \left(\boldsymbol{w}_t + \eta \left(e^{-y_t^{(1)}} \boldsymbol{x}_1 + e^{-y_t^{(2)}} \boldsymbol{x}_2 \right) \right)^\top \boldsymbol{x}_1 \\ \qquad = y_t^{(1)} + \eta e^{-y_t^{(1)}} \|\boldsymbol{x}_1\|^2 + \eta e^{-y_t^{(2)}} \langle \boldsymbol{x}_1, \boldsymbol{x}_2 \rangle, \\ y_{t+1}^{(2)} = y_t^{(2)} + \eta e^{-y_t^{(2)}} \|\boldsymbol{x}_2\|^2 + \eta e^{-y_t^{(1)}} \langle \boldsymbol{x}_1, \boldsymbol{x}_2 \rangle. \end{cases} \tag{8}$$

Assume that $\boldsymbol{x}_2$ is farther from the origin in terms of distance than $\boldsymbol{x}_1$ is, but not too different in terms of angle. Formally,

Assumption D.1. $\|\boldsymbol{x}_2\| > 1$, $4\|\boldsymbol{x}_1\|^2 < 2\langle \boldsymbol{x}_1, \boldsymbol{x}_2 \rangle < \|\boldsymbol{x}_2\|^2$. Moreover, $\langle \boldsymbol{x}_1, \boldsymbol{x}_2 \rangle < \|\boldsymbol{x}_1\| \|\boldsymbol{x}_2\|$.

Under these assumptions, as $\langle \boldsymbol{x}_1, \boldsymbol{x}_2 \rangle > 0$, $\mathcal{D}$ is linearly separable. Also, notice that $\boldsymbol{x}_1$ and $\boldsymbol{x}_2$ are not parallel. Our definition of a linearly separable dataset is in accordance with Soudry et al. (2018). A dataset $\mathcal{D}$ is linearly separable if there exists $\boldsymbol{w}^*$ such that $\langle \boldsymbol{x}_i, \boldsymbol{w}^* \rangle > 0, \forall i$.

Theorem D.2. *Let $V_{t;J}^{(i)}$ be the variance and $\mu_{t;J}^{(i)}$ be the mean of $\sigma(y_t^{(i)})$ within a window from time t to $t + J - 1$. Denote T_v and T_{vm} as the first time when $V_{t;J}^{(1)} > V_{t;J}^{(2)}$ and $V_{t;J}^{(1)}(1 - \mu_{t;J}^{(i)}) > V_{t;J}^{(2)}(1 - \mu_{t;J}^{(2)})$ occurs, respectively. Under Assumption D.1, if η is sufficiently small then $T_{vm} < T_v$.*

By Soudry et al. (2018), the learning is progressed as: $\boldsymbol{w}_t$, $y_t^{(1)}$, and $y_t^{(2)}$ diverges to positive infinity (Lemma 1) but $\boldsymbol{w}_t$ directionally converges towards L_2 max margin vector, $\hat{\boldsymbol{w}} = \boldsymbol{x}_1 / \|\boldsymbol{x}_1\|^2$, or $\lim_{t \to \infty} \frac{\boldsymbol{w}_t}{\|\boldsymbol{w}_t\|} = \frac{\hat{\boldsymbol{w}}}{\|\hat{\boldsymbol{w}}\|}$ (Theorem 3). Moreover, the growth of $\boldsymbol{w}$ is logarithmic, i.e. $\boldsymbol{w}_t \approx \hat{\boldsymbol{w}} \log t$. We hereby note that Theorem 3 of Soudry et al. (2018) holds for learning rate η smaller than a global constant. Since our condition requires η to be sufficiently small, we will make use of the findings of Theorem 3.

Lemma D.3. $\Delta y_t := y_t^{(2)} - y_t^{(1)}$ *is a non-negative, strictly increasing sequence. Also,* $\lim_{t \to \infty} \Delta y_t = \infty$.

Proof.

1) Since $\boldsymbol{w}_0 = 0$, $y_0^{(1)} = 0 = y_0^{(2)}$ so $\Delta y_0 = 0$. By Equation (8) and Assumption D.1, $\Delta y_1 = y_1^{(2)} - y_1^{(1)} = \eta\left(\|\boldsymbol{x}_2\|^2 - \|\boldsymbol{x}_1\|^2\right) > 0$.

2)

$$\begin{aligned}\Delta y_{t+1} - \Delta y_t &= \eta\left[e^{-y_t^{(2)}}\left(\|\boldsymbol{x}_2\|^2 - \langle \boldsymbol{x}_1, \boldsymbol{x}_2\rangle\right) + e^{-y_t^{(1)}}\left(\langle \boldsymbol{x}_1, \boldsymbol{x}_2\rangle - \|\boldsymbol{x}_1\|^2\right)\right] \\ &=: K_1 e^{-y_t^{(1)}} + K_2 e^{-y_t^{(2)}} > 0,\end{aligned}$$

for some positive constant K_1, K_2. As $y_t^{(i)} = \boldsymbol{w}_t^\top \boldsymbol{x}_i$ would logarithmically grow in terms of t, $e^{-y_t^{(i)}}$ is decreasing in t. Moreover, as $y_t^{(1)} = \boldsymbol{w}_t^\top \boldsymbol{x}_1 \approx \hat{\boldsymbol{w}}^\top \boldsymbol{x}_1 \log t = \log t$, $e^{-y_t^{(1)}}$ is (asymptotically) in scale of t^{-1} and so is $\Delta y_{t+1} - \Delta y_t$. Hence, $\{\Delta y_t\}$ is non-negative and increases to infinity. □

The notation $\Delta y_t \coloneqq y_t^{(2)} - y_t^{(1)}$ will be used throughout this section. Next, we show that, under Assumption D.1, $y_{t+1}^{(1)} < y_t^{(2)}$ for all $t > 0$.

Lemma D.4. *For all $t > 0$, $y_{t+1}^{(1)} < y_t^{(2)}$.*

Proof. Notice that:

$$\begin{cases} y_1^{(1)} = \eta\|\boldsymbol{x}_1\|^2 + \eta\langle \boldsymbol{x}_1, \boldsymbol{x}_2\rangle \\ y_1^{(2)} = \eta\|\boldsymbol{x}_2\|^2 + \eta\langle \boldsymbol{x}_1, \boldsymbol{x}_2\rangle. \end{cases}$$

1) $y_2^{(1)} < y_1^{(2)}$:

$$\begin{aligned} y_2^{(1)} &= y_1^{(1)} + \eta e^{-y_1^{(1)}}\|\boldsymbol{x}_1\|^2 + \eta e^{-y_1^{(2)}}\langle \boldsymbol{x}_1, \boldsymbol{x}_2\rangle \\ &= \eta\left(e^{-y_1^{(1)}} + 1\right)\|\boldsymbol{x}_1\|^2 + \eta\left(e^{-y_1^{(2)}} + 1\right)\langle \boldsymbol{x}_1, \boldsymbol{x}_2\rangle \\ &< \eta \times 2\|\boldsymbol{x}_1\|^2 + \eta \times 2\langle \boldsymbol{x}_1, \boldsymbol{x}_2\rangle \\ &< \eta\langle \boldsymbol{x}_1, \boldsymbol{x}_2\rangle + \eta\|\boldsymbol{x}_2\|^2 = y_1^{(2)}. \end{aligned}$$

2) Assume, for $t > 0$, $y_{t+1}^{(1)} < y_t^{(2)}$.

$$\begin{aligned} y_{t+2}^{(1)} &= y_{t+1}^{(1)} + \eta e^{-y_{t+1}^{(1)}}\|\boldsymbol{x}_1\|^2 + \eta e^{-y_{t+1}^{(2)}}\langle \boldsymbol{x}_1, \boldsymbol{x}_2\rangle \\ &< y_t^{(2)} + \eta e^{-y_t^{(1)}}\|\boldsymbol{x}_1\|^2 + \eta e^{-y_t^{(2)}}\langle \boldsymbol{x}_1, \boldsymbol{x}_2\rangle \\ &< y_t^{(2)} + \eta e^{-y_t^{(1)}}\langle \boldsymbol{x}_1, \boldsymbol{x}_2\rangle + \eta e^{-y_t^{(2)}}\|\boldsymbol{x}_2\|^2 = y_{t+1}^{(2)}. \end{aligned}$$

□

By Lemma D.4, for all $t > 0$, $\left(y_t^{(2)}, y_{t+1}^{(2)}\right)$ lies entirely on right-hand side of $\left(y_t^{(1)}, y_{t+1}^{(1)}\right)$, without any overlap.

We first analyze the following term: $\frac{y_{t+1}^{(1)} - y_t^{(1)}}{y_{t+1}^{(2)} - y_t^{(2)}}$. Observe that:

$$\begin{aligned} \frac{y_{t+1}^{(1)} - y_t^{(1)}}{y_{t+1}^{(2)} - y_t^{(2)}} &= \frac{\eta e^{-y_t^{(1)}}\|\boldsymbol{x}_1\|^2 + \eta e^{-y_t^{(2)}}\langle \boldsymbol{x}_1, \boldsymbol{x}_2\rangle}{\eta e^{-y_t^{(2)}}\|\boldsymbol{x}_2\|^2 + \eta e^{-y_t^{(1)}}\langle \boldsymbol{x}_1, \boldsymbol{x}_2\rangle} \\ &= \frac{\|\boldsymbol{x}_1\|^2 + e^{-\Delta y_t}\langle \boldsymbol{x}_1, \boldsymbol{x}_2\rangle}{\langle \boldsymbol{x}_1, \boldsymbol{x}_2\rangle + e^{-\Delta y_t}\|\boldsymbol{x}_2\|^2}. \end{aligned} \tag{9}$$

It is derived that the fraction is an increasing sequence in terms of t. For values $a, b, c, c', d, d' > 0$, $\frac{a+c}{b+d} < \frac{a+c'}{b+d'} \Leftrightarrow ad' + cb + cd' < ad + c'b + c'd$. Taking:

$$\begin{cases} a = \|\boldsymbol{x}_1\|^2 \\ b = \langle \boldsymbol{x}_1, \boldsymbol{x}_2 \rangle \end{cases} \quad \begin{cases} c = e^{-\Delta y_t} \langle \boldsymbol{x}_1, \boldsymbol{x}_2 \rangle \\ d = e^{-\Delta y_t} \|\boldsymbol{x}_2\|^2 \end{cases} \quad \begin{cases} c' = e^{-\Delta y_{t+1}} \langle \boldsymbol{x}_1, \boldsymbol{x}_2 \rangle \\ d' = e^{-\Delta y_{t+1}} \|\boldsymbol{x}_2\|^2 \end{cases},$$

we have

$$\begin{aligned} & ad' + cb + cd' \\ &= e^{-\Delta y_{t+1}} \|\boldsymbol{x}_1\|^2 \|\boldsymbol{x}_2\|^2 + e^{-\Delta y_t} \langle \boldsymbol{x}_1, \boldsymbol{x}_2 \rangle^2 + e^{-\Delta y_t} e^{-\Delta y_{t+1}} \langle \boldsymbol{x}_1, \boldsymbol{x}_2 \rangle \|\boldsymbol{x}_2\|^2 \\ &< e^{-\Delta y_t} \|\boldsymbol{x}_1\|^2 \|\boldsymbol{x}_2\|^2 + e^{-\Delta y_{t+1}} \langle \boldsymbol{x}_1, \boldsymbol{x}_2 \rangle^2 + e^{-\Delta y_t} e^{-\Delta y_{t+1}} \langle \boldsymbol{x}_1, \boldsymbol{x}_2 \rangle \|\boldsymbol{x}_2\|^2 \\ &= ad + c'b + c'd. \end{aligned}$$

The inequality holds by Lemma D.3 and the Cauchy-Schwarz inequality. Taking the limit of Equation (9) as $t \to \infty$, the ratio converges to:

$$R \coloneqq \frac{\|\boldsymbol{x}_1\|^2}{\langle \boldsymbol{x}_1, \boldsymbol{x}_2 \rangle}. \tag{10}$$

For the later uses, we also define the initial ratio, which is smaller than 1:

$$R_0 \coloneqq \frac{y_1^{(1)} - y_0^{(1)}}{y_1^{(2)} - y_0^{(2)}} = \frac{\|\boldsymbol{x}_1\|^2 + \langle \boldsymbol{x}_1, \boldsymbol{x}_2 \rangle}{\langle \boldsymbol{x}_1, \boldsymbol{x}_2 \rangle + \|\boldsymbol{x}_2\|^2} \ (\leq R). \tag{11}$$

Now we analyze a similar ratio of the one-step difference, but in terms of $\sigma\left(y_t^{(i)}\right)$ instead of $y_t^{(i)}$. There, σ stands for the logistic function, $\sigma(z) = (1 + e^{-z})^{-1}$. Notice that $\sigma'(z) = \sigma(z)(1 - \sigma(z))$.

Lemma D.5. $\gamma_V(t) \coloneqq \frac{\sigma\left(y_{t+1}^{(1)}\right) - \sigma\left(y_t^{(1)}\right)}{\sigma\left(y_{t+1}^{(2)}\right) - \sigma\left(y_t^{(2)}\right)}$ *monotonically increases to* $+\infty$.

Proof.

$$\begin{aligned} \gamma_V(t) &= \frac{y_{t+1}^{(1)} - y_t^{(1)}}{y_{t+1}^{(2)} - y_t^{(2)}} \frac{\sigma'\left(\zeta_t^{(1)}\right)}{\sigma'\left(\zeta_t^{(2)}\right)} \quad \left(\text{for some } \begin{cases} \zeta_t^{(1)} \in \left(y_t^{(1)}, y_{t+1}^{(1)}\right) \\ \zeta_t^{(2)} \in \left(y_t^{(2)}, y_{t+1}^{(2)}\right) \end{cases} \text{by the mean value theorem.}\right) \\ &\geq \frac{y_{t+1}^{(1)} - y_t^{(1)}}{y_{t+1}^{(2)} - y_t^{(2)}} \frac{\sigma'\left(y_{t+1}^{(1)}\right)}{\sigma'\left(y_t^{(2)}\right)} \quad (\because \sigma' \text{: decreasing on } \mathbb{R}^+) \\ &= \frac{y_{t+1}^{(1)} - y_t^{(1)}}{y_{t+1}^{(2)} - y_t^{(2)}} \frac{e^{-y_{t+1}^{(1)}} \left(1 + e^{-y_{t+1}^{(1)}}\right)^{-2}}{e^{-y_t^{(2)}} \left(1 + e^{-y_t^{(2)}}\right)^{-2}} \\ &\geq \frac{y_{t+1}^{(1)} - y_t^{(1)}}{y_{t+1}^{(2)} - y_t^{(2)}} \frac{1}{4} e^{y_t^{(2)} - y_{t+1}^{(1)}} \quad (\because \left(1 + e^{-z}\right)^{-2} \in [1/4, 1] \text{ on } \mathbb{R}^+) \\ &\geq \frac{R_0}{4} e^{y_t^{(2)} - y_{t+1}^{(1)}}. \end{aligned}$$

As $y_t^{(2)} - y_{t+1}^{(1)} = y_t^{(2)} - y_t^{(1)} - \eta\left(e^{-y_t^{(1)}} \|\boldsymbol{x}_1\|^2 + e^{-y_t^{(2)}} \langle \boldsymbol{x}_1, \boldsymbol{x}_2 \rangle\right) \to \infty$, $\gamma_V(t) \to \infty$. For the part that proves $\gamma_V(t)$ is increasing, see Appendix D.1.1. □

Notice that $\gamma_V(0) < 1$. Lemma D.5 implies that there exists (unique) $T_v > 0$ such that for all $t \geq T_v$, $\gamma_V(t) > 1$ holds, or $\sigma\left(y_{t+1}^{(1)}\right) - \sigma\left(y_t^{(1)}\right) > \sigma\left(y_{t+1}^{(2)}\right) - \sigma\left(y_t^{(2)}\right)$. Recall that the (sample) variance of a finite dataset $\mathcal{T} = \{\boldsymbol{x}_1, \cdots, \boldsymbol{x}_n\}$ can be computed as:

$$\mathrm{Var}[\mathcal{T}] = \frac{1}{n(n-1)} \sum_{i=1}^{n-1} \sum_{j=i+1}^{n} (\boldsymbol{x}_i - \boldsymbol{x}_j)^2.$$

Hence, for given J, (which corresponds to the window size,) for all $t \geq T_v$,

$$\begin{aligned} V_{t;J}^{(1)} \coloneqq \mathrm{Var}\left[\left\{\sigma\left(y_\tau^{(1)}\right)\right\}_{\tau=t}^{t+J-1}\right] &= \frac{1}{J(J-1)}\sum_{k=0}^{J-2}\sum_{l=k+1}^{J-1}\left[\sigma\left(y_{t+l}^{(1)}\right)-\sigma\left(y_{t+k}^{(1)}\right)\right]^2 \\ &> \frac{1}{J(J-1)}\sum_{k=0}^{J-2}\sum_{l=k+1}^{J-1}\left[\sigma\left(y_{t+l}^{(2)}\right)-\sigma\left(y_{t+k}^{(2)}\right)\right]^2 \\ &= \mathrm{Var}\left[\left\{\sigma\left(y_\tau^{(2)}\right)\right\}_{\tau=t}^{t+J-1}\right] =: V_{t;J}^{(2)}. \end{aligned}$$

It is easily derived that the converse is true: If $\gamma_V(t)$ is increasing and $V_{t;J}^{(1)} > V_{t;J}^{(2)}$ then $\gamma_V(t) > 1$.

We have two metrics: the first is only the variance (which corresponds to the Dyn-Unc score) and the second is the variance multiplied by the mean subtracted from 1 (which corresponds to the DUAL pruning score). Both the variance and the mean are calculated within a window of fixed length. At the early epoch, as the model learns $\boldsymbol{x}_2$ first, both metrics show a smaller value for $\boldsymbol{x}_1$ than that for $\boldsymbol{x}_2$. At the late epoch, now the model learns $\boldsymbol{x}_1$, so the order of the metric values reverses for both metrics.

Our goal is to show that the elapsed time of the second metric for the order to be reversed is shorter than that of the first metric. Let T_{vm} be that time for our metric. We represent the mean of the logistic output within a window of length J and from epoch t, computed for i-th instance by $\mu_{t;J}^{(i)}$:

$$\mu_{t;J}^{(i)} \coloneqq \frac{1}{J}\sum_{\tau=t}^{t+J-1}\sigma\left(y_\tau^{(i)}\right). \tag{12}$$

For $t \geq T_v$, we see that the inequality still holds:

$$\begin{aligned} &V_{t;J}^{(1)}\left(1-\mu_{t;J}^{(1)}\right) \\ &= \left[\frac{1}{J(J-1)}\sum_{k=0}^{J-2}\sum_{l=k+1}^{J-1}\left[\sigma\left(y_{t+l}^{(1)}\right)-\sigma\left(y_{t+k}^{(1)}\right)\right]^2\right]\left[1-\frac{1}{J}\sum_{\tau=t}^{t+J-1}\sigma\left(y_\tau^{(1)}\right)\right] \\ &> \left[\frac{1}{J(J-1)}\sum_{k=0}^{J-2}\sum_{l=k+1}^{J-1}\left[\sigma\left(y_{t+l}^{(2)}\right)-\sigma\left(y_{t+k}^{(2)}\right)\right]^2\right]\left[1-\frac{1}{J}\sum_{\tau=t}^{t+J-1}\sigma\left(y_\tau^{(2)}\right)\right] \\ &= V_{t;J}^{(2)}\left(1-\mu_{t;J}^{(2)}\right). \end{aligned}$$

as for all t, $\sigma\left(y_t^{(2)}\right) > \sigma\left(y_t^{(1)}\right)$. Indeed, $T_{vm} \leq T_v$ holds, but is $T_{vm} < T_v$ true? To verify the question, we reshape the terms for a similar analysis upon μ:

$$\begin{aligned} &V_{t;J}^{(1)}\left(1-\mu_{t;J}^{(1)}\right) \\ &= \left[\frac{1}{J(J-1)}\sum_{k=0}^{J-2}\sum_{l=k+1}^{J-1}\left[\sigma\left(y_{t+l}^{(1)}\right)-\sigma\left(y_{t+k}^{(1)}\right)\right]^2\right]\left[\frac{1}{J}\sum_{\tau=t}^{t+J-1}1-\sigma\left(y_\tau^{(1)}\right)\right] \\ &> \left[\frac{1}{J(J-1)}\sum_{k=0}^{J-2}\sum_{l=k+1}^{J-1}\left[\sigma\left(y_{t+l}^{(2)}\right)-\sigma\left(y_{t+k}^{(2)}\right)\right]^2\right]\left[\frac{1}{J}\sum_{\tau=t}^{t+J-1}1-\sigma\left(y_\tau^{(2)}\right)\right] \\ &= V_{t;J}^{(2)}\left(1-\mu_{t;J}^{(2)}\right). \end{aligned} \tag{13}$$

The intuition is now clear: for any time before T_v, we know that the variance of $\boldsymbol{x}_1$ is smaller than that of $\boldsymbol{x}_2$, if the ratio corresponding to $1-\sigma(y)$ is large, the factors could be canceled out and the inequality still holds. If this case is possible, definitely $T_{vm} < T_v$.

Now let us analyze the ratio of $1-\sigma\left(y_t^{(i)}\right)$.

Lemma D.6. $\gamma_M(t) \coloneqq \frac{1-\sigma\left(y_t^{(1)}\right)}{1-\sigma\left(y_t^{(2)}\right)}$ *increases to* $+\infty$.

Proof.

$$\begin{aligned}\gamma_M(t) &= \frac{1+e^{y_t^{(2)}}}{1+e^{y_t^{(1)}}} \\ &= e^{\Delta y_t} - \frac{e^{\Delta y_t}-1}{1+e^{y_t^{(1)}}} \\ &\geq e^{\Delta y_t} - \frac{e^{\Delta y_t}}{1+e^{y_t^{(1)}}} \\ &= e^{\Delta y_t}\sigma\left(y_t^{(1)}\right).\end{aligned}$$

The quantity in the last line indeed diverges to infinity. We now show that $\gamma_M(t)$ is increasing.

$$\begin{aligned}\gamma_M(t) &= e^{\Delta y_t} - \frac{e^{\Delta y_t}}{1+e^{y_t^{(1)}}} + \frac{1}{1+e^{y_t^{(1)}}} \\ &= e^{\Delta y_t}\sigma\left(y_t^{(1)}\right) + 1 - \sigma\left(y_t^{(1)}\right) \\ &= \left(e^{\Delta y_t}-1\right)\sigma\left(y_t^{(1)}\right) + 1 \\ &< \left(e^{\Delta y_{t+1}}-1\right)\sigma\left(y_{t+1}^{(1)}\right) + 1 = \gamma_M(t+1).\end{aligned}$$

□

Notice that, for $a > c > 0, b > d > 0, \frac{a-c}{b-d} < \frac{a}{b} \Leftrightarrow \frac{a}{b} < \frac{c}{d}$. Recall from Lemma D.5 that $\gamma_V(t) = \frac{1-\sigma\left(y_t^{(1)}\right)-\left[1-\sigma\left(y_{t+1}^{(1)}\right)\right]}{1-\sigma\left(y_t^{(2)}\right)-\left[1-\sigma\left(y_{t+1}^{(2)}\right)\right]}$, hence $\gamma_V(t) < \gamma_M(t)$. Moreover,

$$\begin{aligned}\gamma_V(t) &\leq \frac{y_{t+1}^{(1)}-y_t^{(1)}}{y_{t+1}^{(2)}-y_t^{(2)}}\frac{\sigma'\left(y_t^{(1)}\right)}{\sigma'\left(y_{t+1}^{(2)}\right)} \\ &= \frac{y_{t+1}^{(1)}-y_t^{(1)}}{y_{t+1}^{(2)}-y_t^{(2)}}e^{y_{t+1}^{(2)}-y_t^{(1)}}\left(\frac{1+e^{-y_{t+1}^{(2)}}}{1+e^{-y_t^{(1)}}}\right)^2 \\ &\leq \frac{y_{t+1}^{(1)}-y_t^{(1)}}{y_{t+1}^{(2)}-y_t^{(2)}}e^{y_{t+1}^{(2)}-y_t^{(1)}}\left(\frac{1+e^{-y_{t+1}^{(2)}}}{1+e^{-y_t^{(1)}}}\right) \quad \because \left(\frac{1+e^{-y_{t+1}^{(2)}}}{1+e^{-y_t^{(1)}}}\right) \in (0,1]. \\ &= \frac{y_{t+1}^{(1)}-y_t^{(1)}}{y_{t+1}^{(2)}-y_t^{(2)}}e^{y_{t+1}^{(2)}-y_t^{(2)}}e^{\Delta y_t}\left(\frac{1+e^{-y_{t+1}^{(2)}}}{1+e^{-y_t^{(1)}}}\right) \\ &\leq \frac{y_{t+1}^{(1)}-y_t^{(1)}}{y_{t+1}^{(2)}-y_t^{(2)}}e^{y_{t+1}^{(2)}-y_t^{(2)}}e^{\Delta y_t}\left(\frac{1+e^{-y_t^{(2)}}}{1+e^{-y_t^{(1)}}}\right) \\ &\leq Re^{y_1^{(2)}-y_0^{(2)}}\gamma_M(t).\end{aligned}$$

Now we revisit Equation (13).

$$\begin{aligned}&\left[\frac{1}{J(J-1)}\sum_{k=0}^{J-2}\sum_{l=k+1}^{J-1}\left[\sigma\left(y_{t+l}^{(1)}\right)-\sigma\left(y_{t+k}^{(1)}\right)\right]^2\right]\left[\frac{1}{J}\sum_{\tau=t}^{t+J-1}1-\sigma\left(y_\tau^{(1)}\right)\right] \\ >&\left[\frac{1}{J(J-1)}\sum_{k=0}^{J-2}\sum_{l=k+1}^{J-1}\left[\sigma\left(y_{t+l}^{(2)}\right)-\sigma\left(y_{t+k}^{(2)}\right)\right]^2\right]\left[\frac{1}{J}\sum_{\tau=t}^{t+J-1}1-\sigma\left(y_\tau^{(2)}\right)\right].\end{aligned} \tag{14}$$

Assume, for the moment, that for some constant $C > 1$, $\sigma\left(y_{t+1}^{(1)}\right) - \sigma\left(y_t^{(1)}\right) > C^{-1}\left[\sigma\left(y_{t+1}^{(2)}\right) - \sigma\left(y_t^{(2)}\right)\right]$ but $1-\sigma\left(y_t^{(1)}\right) > C^2\left[1-\sigma\left(y_t^{(2)}\right)\right]$ for all large t. Then the ratio of the first term of the left-hand side of Equation (14) to the first term of the right-hand side is greater than C^{-2}. Also, the ratio of the second term of the left-hand side of Equation (14) to the second term of the right-hand side is greater than C^2. If so, we observe that 1) the inequality in Equation (14) holds, 2) as the condition $\gamma_V(t) \geq 1$ for T_v now changed to $\gamma_V(t) \geq C^{-1}$ for T_{vm}, hence $T_{vm} < T_v$ is guaranteed. It remains to find the constant C. Recall that, for all t,

$$\gamma_V(t) \leq Re^{y_1^{(2)} - y_0^{(2)}} \gamma_M(t).$$

If we set $Re^{y_1^{(2)} - y_0^{(2)}} = C^{-3}$, when $\gamma_V(t)$ becomes at least C^{-1}, we have $\gamma_M(t) \geq C^2$, satisfying the condition for T_{vm}. If the learning rate is sufficiently small, then $\gamma_V(t)$ cannot significantly increase in one step, allowing $\gamma_V(t)$ to fall between C^{-1} and 1. Refer to Figure 18a to observe that the graph of $\gamma_V(t)$ resembles that of a continuously increasing function.

D.1.1 Monotonicity of $\gamma_V(t)$

Recall that:

$$\begin{aligned}\gamma_V(t) &\coloneqq \frac{\sigma\left(y_{t+1}^{(1)}\right) - \sigma\left(y_t^{(1)}\right)}{\sigma\left(y_{t+1}^{(2)}\right) - \sigma\left(y_t^{(2)}\right)} \\ &= \frac{y_{t+1}^{(1)} - y_t^{(1)}}{y_{t+1}^{(2)} - y_t^{(2)}} \frac{\sigma'\left(\zeta_t^{(1)}\right)}{\sigma'\left(\zeta_t^{(2)}\right)}\end{aligned}$$

for some $\zeta_t^{(1)} \in \left(y_t^{(1)}, y_{t+1}^{(1)}\right), \zeta_t^{(2)} \in \left(y_t^{(2)}, y_{t+1}^{(2)}\right)$ by the mean value theorem. The first term is shown to be increasing (to R). $\gamma_V(t)$ is increasing if the second term is also increasing in t.

Let $\Delta\zeta_t \coloneqq \zeta_t^{(2)} - \zeta_t^{(1)}$. By Lemma D.4, $\Delta\zeta_t > 0$.

$$\begin{aligned}\frac{\sigma'\left(\zeta_t^{(1)}\right)}{\sigma'\left(\zeta_t^{(2)}\right)} &= \frac{e^{-\zeta_t^{(1)}}}{e^{-\zeta_t^{(2)}}} \left(\frac{1+e^{-\zeta_t^{(2)}}}{1+e^{-\zeta_t^{(1)}}}\right)^2 \\ &= e^{\Delta\zeta_t} \left(\frac{1+e^{-\zeta_t^{(1)} - \Delta\zeta_t}}{1+e^{-\zeta_t^{(1)}}}\right)^2.\end{aligned}$$

Define $g(x,y) \coloneqq e^x \left(\frac{1+e^{-y-x}}{1+e^{-y}}\right)^2$. The partial derivatives satisfy:

$$\begin{cases}\nabla_x g = \frac{\left(e^y - e^{-x}\right)\left(e^{x+y}+1\right)}{(1+e^y)^2} > 0 \text{ for } x > 0 \text{ if } y > 0 \\ \nabla_y g = \frac{2e^{y-x}(e^x-1)\left(e^{x+y}+1\right)}{(1+e^y)^3} > 0, \forall y \text{ if } x > 0.\end{cases}$$

Notice that $\frac{\sigma'\left(\zeta_t^{(1)}\right)}{\sigma'\left(\zeta_t^{(2)}\right)} = g(\Delta\zeta_t, \zeta_t^{(1)})$. Since $\zeta_t^{(1)} \in \left(y_t^{(1)}, y_{t+1}^{(1)}\right)$ is (strictly) increasing and positive, if we show that $\Delta\zeta_t$ is increasing in t, we are done. Our result is that, if $y_{t+1}^{(i)} - y_t^{(i)}$ is small for $i = 1, 2$, $\zeta_t^{(i)} \approx \left(y_t^{(i)} + y_{t+1}^{(i)}\right)/2$ so $\Delta\zeta_t \approx \left(\Delta y_t + \Delta y_{t+1}\right)/2$, which is indeed increasing.

In particular, if (, assume for now) for all t,

$$\begin{aligned}
\zeta_t^{(i)} &\in \left(\frac{2y_t^{(i)} + y_{t+1}^{(i)}}{3}, \frac{y_t^{(i)} + 2y_{t+1}^{(i)}}{3}\right) && (15)\\
\Rightarrow\ \Delta\zeta_t &\in \left(\frac{\Delta y_t + \Delta y_{t+1}}{3} + \frac{y_t^{(2)} - y_{t+1}^{(1)}}{3}, \frac{\Delta y_t + \Delta y_{t+1}}{3} + \frac{y_{t+1}^{(2)} - y_t^{(1)}}{3}\right)\\
\Rightarrow\ \Delta\zeta_t &< \frac{\Delta y_t + \Delta y_{t+1}}{3} + \frac{y_{t+1}^{(2)} - y_t^{(1)}}{3}\\
&< \frac{\Delta y_{t+1} + \Delta y_{t+2}}{3} + \frac{y_{t+1}^{(2)} - y_{t+2}^{(1)}}{3} && (\dagger)\\
&< \Delta\zeta_{t+1}
\end{aligned}$$

$(\dagger)$ holds by Assumption D.1:

$$\begin{aligned}
(\dagger) &\Leftrightarrow \Delta y_{t+2} - \Delta y_t > y_{t+2}^{(1)} - y_t^{(1)}, \forall t\\
&\Leftarrow \Delta y_{t+1} - \Delta y_t > y_{t+1}^{(1)} - y_t^{(1)}, \forall t\\
&\Leftrightarrow \eta\left[e^{-y_t^{(1)}}\left(\langle \boldsymbol{x}_1, \boldsymbol{x}_2\rangle - \|\boldsymbol{x}_1\|^2\right) + e^{-y_t^{(2)}}\left(\|\boldsymbol{x}_2\|^2 - \langle \boldsymbol{x}_1, \boldsymbol{x}_2\rangle\right)\right] >\\
&\quad \eta\left[e^{-y_t^{(1)}}\|\boldsymbol{x}_1\|^2 + e^{-y_t^{(2)}}\langle \boldsymbol{x}_1, \boldsymbol{x}_2\rangle\right], \forall t.
\end{aligned}$$

It remains to show Equation (15). To this end, we use Lemma D.7.

Lemma D.7. *Let $z_2 > z_1 (\geq 0)$ be reals and $\zeta \in (z_1, z_2)$ be a number that satisfies the following: $\sigma(z_2) - \sigma(z_1) = (z_2 - z_1)\sigma'(\zeta)$. Denote the midpoint of (z_1, z_2) as $m := (z_1 + z_2)/2$. For $(1 \gg)\epsilon > 0$, if $z_2 - z_1 < \mathcal{O}(\sqrt{\epsilon})$ then $|\zeta - m| < \epsilon$.*

Proof. Expand the Taylor series of σ at m for z_i:

$$\sigma(z_i) = \sigma(m) + \sigma'(m)(z_i - m) + \frac{1}{2!}\sigma''(m)(z_i - m)^2 + \frac{1}{3!}\sigma'''(m)(z_i - m)^3 + \mathcal{O}\left(|z_i - m|^4\right)$$

We have:

$$\sigma(z_2) - \sigma(z_1) = \sigma'(m)(z_2 - z_1) + \frac{1}{24}\sigma'''(m)(z_2 - z_1)^3 + \mathcal{O}\left((z_2 - z_1)^5\right)$$

$$\sigma'(\zeta) = \sigma'(m) + \frac{1}{24}\sigma'''(m)(z_2 - z_1)^2 + \mathcal{O}\left((z_2 - z_1)^4\right)$$

Now, expand the Taylor series of σ' at m for ζ:

$$\sigma'(\zeta) = \sigma'(m) + \sigma''(m)(\zeta - m) + \frac{1}{2!}\sigma'''(m)(\zeta - m)^2 + \mathcal{O}\left(|\zeta - m|^3\right)$$

Comparing the above two lines gives

$$24\sigma''(m)(\zeta - m) + 12\sigma'''(m)(\zeta - m)^2 = \sigma'''(m)(z_2 - z_1)^2 + \mathcal{O}\left((z_2 - z_1)^3\right)$$

If $\sigma'''(m) = 0$ then $|\zeta - m| = \mathcal{O}\left((z_2 - z_1)^3\right)$, so $z_2 - z_1 = \mathcal{O}(\sqrt{\epsilon})$ is sufficient.

Otherwise, we can solve the above for $\zeta - m$ from the fact that $\sigma''(z) < 0$ for $z > 0$:

$$\begin{aligned}
12\sigma'''(m)(\zeta - m) &= -12\sigma''(m) - \sqrt{(12\sigma''(m))^2 + 12\sigma'''(m)\left[\sigma'''(m)(z_2 - z_1)^2 + \mathcal{O}\left((z_2 - z_1)^3\right)\right]}\\
&= \frac{12\sigma'''(m)^2(z_2 - z_1)^2}{24\sigma''(m)} + \mathcal{O}\left((z_2 - z_1)^3\right)
\end{aligned}$$

The last equality is from the Taylor series $\sqrt{1 + \frac{a}{x^2}} - 1 = \frac{a}{2x^2} + \mathcal{O}\left(a^2x^{-4}\right)$, or $\sqrt{x^2 + a} - x = \frac{a}{2x} + \mathcal{O}\left(a^2x^{-3}\right)$. We have $|\zeta - m| = \Theta\left((z_2 - z_1)^2\right)$. $\square$

For $|\zeta_t^{(i)} - \left(y_t^{(i)} + y_{t+1}^{(i)}\right)/2| < \left(y_{t+1}^{(i)} - y_t^{(i)}\right)/6$, it suffices to have $y_{t+1}^{(i)} - y_t^{(i)} < \mathcal{O}\left(\sqrt{\left(y_{t+1}^{(i)} - y_t^{(i)}\right)/6}\right)$. This generally holds for sufficiently small η.

D.2 Experimental Results under Synthetic Setting

This section displays the figures plotted from the experiments on the synthetic dataset. We choose $\mathcal{X} = \mathbb{R}^2$ and $\mathcal{D} = \{\ ((0.1, 0.1), 1), ((10, 5), 1)\}$. We fix $J = 10$ and $\eta = 0.01$ (unless specified). The total time of training T is specified for each figure for neat visualization. In this setting, the upper bound for the learning rate is $\log(75)/126.5 \approx 0.034$.

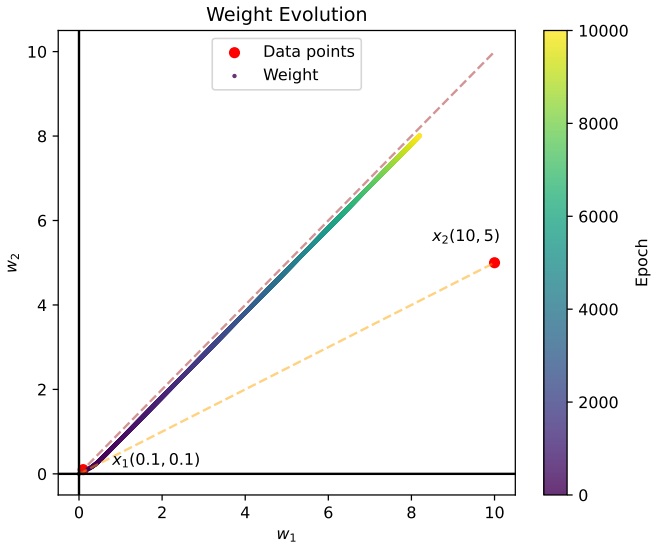

Figure 17: Illustration of the evolution of the weight as the model learns from the two-point dataset. Observe that the weight learns $\boldsymbol{x}_2$ first (closer to the orange dashed line), but gradually moves towards $\boldsymbol{x}_1$ (closer to the brown dashed line). Here $T = 10,000$.

We also empirically validate our statements of Appendix D.1.1. Figure 18 shows that $\gamma_V(t)$ and $\Delta\zeta_t$ are indeed increasing functions. Figure 19 shows that $\zeta_t^{(i)}$ is sufficiently close to the midpoint of the interval it lies in, $\left(y_t^{(i)}, y_{t+1}^{(i)}\right)$.

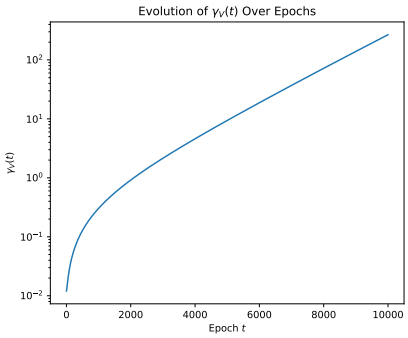

(a) $\gamma_V(t)$ in log scale.

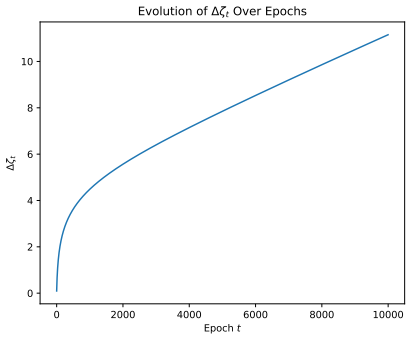

(b) $\Delta\zeta_t$

Figure 18: Empirical validations of the critical statements in Appendix D.1.1. We ran experiments and plot the results that both $\gamma_V(t)$ (left—in log scale) and $\Delta\zeta_t$ (right) are an increasing sequence in terms of t. Here, we set $\eta = 0.0005$. The reason is that if the learning rate is larger, $\sigma(y_t^{(2)})$ quickly saturates to 1, leading to a possibility of division by zero in $\gamma_V(t)$ and degradation in numerical stability of $\Delta\zeta_t$. Moreover, notice that the graph of $\gamma_V(t)$ in the log scale closely resembles that of $\Delta\zeta_t$ in the original scale.

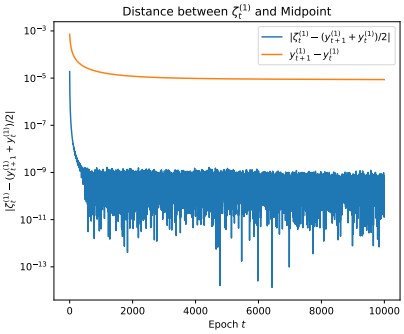

(a) $|\zeta_t^{(1)} - (y_t^{(1)} + y_{t+1}^{(1)})/2|$ in log scale.

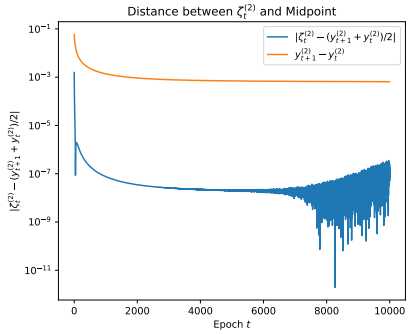

(b) $|\zeta_t^{(2)} - (y_t^{(2)} + y_{t+1}^{(2)})/2|$ in log scale.

Figure 19: Empirical validations of the critical statements in Appendix D.1.1. We ran experiments and plot the results that both $\zeta_t^{(1)}$ (left) and $\zeta_t^{(2)}$ (right) are extremely close to the midpoint $(y_t^{(1)} + y_{t+1}^{(1)})/2$ and $(y_t^{(2)} + y_{t+1}^{(2)})/2$, compared to the interval length, respectively. In both plots, the blue line is the true distance while the orange line is the interval length. Here, we set $\eta = 0.0005$ for the same reasoning of Figure 18. Empirically, the noise introduced by MVT is too small to deny that $\Delta\zeta_t$ is an increasing sequence.

We also show that we can observe the "flow" of the moon plot as in Figure 2 for the synthetic dataset.

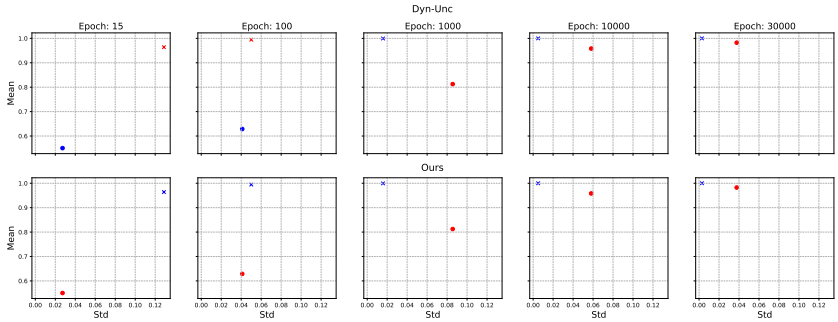

Figure 20: Evolution of $\boldsymbol{x}_1, \boldsymbol{x}_2$ by their mean and standard deviation in prediction probabilities at different epochs. The marker 'o' and 'x' stands for $\boldsymbol{x}_1$ and $\boldsymbol{x}_2$, respectively. The red color indicates the sample to be selected, and the blue color indicates the sample to be pruned. Observe that the path that each data point draws resembles is of moon-shape. Here $T = 30,000$.